

## A domain partitioning based pre-processor for multi-scale modelling of cast aluminium alloys

Somnath Ghosh<sup>1,3</sup>, D M Valivet<sup>4</sup>, Stephen J Harris<sup>2</sup> and James Boileau<sup>2</sup>

<sup>1</sup> Department of Mechanical Engineering, Suite 255, 650 Ackerman Road, The Ohio State University, Columbus, OH 43202, USA

<sup>2</sup> Ford Research Laboratory, Physical and Environmental Sciences Department, MD 3083 SRL, Dearborn, MI 48121-2053, USA

E-mail: [ghosh.5@osu.edu](mailto:ghosh.5@osu.edu)

Received 27 July 2006, in final form 24 October 2006

Published 23 November 2006

Online at [stacks.iop.org/MSMSE/14/1363](http://stacks.iop.org/MSMSE/14/1363)

### Abstract

In this paper, a microstructural morphology based domain partitioning **MDP** methodology is developed for materials with non-uniform heterogeneous microstructure. The comprehensive set of methods is intended to provide a concurrent multi-scale analysis model with an initial computational domain that delineates regions of statistical homogeneity and inhomogeneity. The **MDP** methodology is intended to be a pre-processor to multi-scale analysis of mechanical behaviour and damage of heterogeneous materials, e.g. cast aluminium alloys. It introduces a systematic three-step process that is based on geometric features of morphology. The first step simulates high resolution microstructural information from low resolution micrographs of the material and a limited number of high resolution optical or scanning electron microscopy micrographs. The second step is quantitative characterization of the high resolution images to create effective metrics that can relate microstructural descriptors to material behaviour. The third step invokes a partitioning method to demarcate regions belonging to different length scales in a concurrent multi-scale model. Partitioning criteria for domain partitioning are defined in terms of microstructural descriptors and their functions. The effectiveness of these metrics in differentiating microstructures of a 319-type cast aluminium alloy with different secondary dendrite arm spacings SDAS is demonstrated. The **MDP** method establishes intrinsic material length scales for the different SDAS, namely, 23, 70 and 100  $\mu\text{m}$ , and consequently subdivides the computational domain for concurrently coupling macro- and micromechanical analyses in the multi-scale model.

<sup>3</sup> John B. Nordholt Professor. Author to whom any correspondence should be addressed.

<sup>4</sup> Graduate Research Associate.

## 1. Introduction

Cast aluminium alloys such as the 319-type that are used in automotive systems contain microstructural heterogeneities in the form of silicon particulates, intermetallics, precipitates and voids. Typical processing routes can affect the cooling process and result in strong morphological variations such as irregularities in spatial dispersion including clustering and alignment or irregularities in phase shapes and sizes. Experimental studies on ductile failure in [1–4] have shown that these morphological variations strongly affect microstructural damage nucleation due to particulate cracking and interfacial decohesion, as well as ductile damage growth by matrix rupture due to void growth and coalescence. Argon [5] has shown that particles in clustered regions have a greater propensity towards cracking than those in regions of dilute concentration, since local stresses increase rapidly with reduced distance between neighbouring particles. Experimental work in [6, 7] has demonstrated that larger and longer particles are more prone to cracking and damage accumulation increases with higher dendrite arm spacing. Consequently, modelling these alloys for failure properties such as strain to failure, ductility and fracture toughness requires special attention on the microstructural morphology. Various computational models have been proposed for analysis of the mechanical properties and response of multi-phase materials using simplified representations of the microstructural morphology as unit cell models in, e.g. [8–10]. The predictive capabilities of these models for failure properties in non-uniform microstructures are very limited due to simplification of the critical local features that are critical to failure. A few studies have focused on modelling a more realistic representation of microstructures with non-uniform dispersion of heterogeneities [11–14] by combining digital image processing with microstructure modelling. The microstructure-based Voronoi cell finite element model or VCFEM [13–16] has been shown to offer significant promise in accurate analysis of large microstructural regions with high efficiency. Efforts to model three-dimensional microstructural regions with a larger number of spherical particles have been made in [17, 18].

While advances in modern computing and computational hardware have made possible the analysis of extended microstructural regions with a sizeable number of heterogeneities, modelling structural failure incorporating the entire microstructure is still far from reality. In terms of pure micromechanical analysis this would mean single-scale modelling of the entire microstructure from initiation to failure, accounting for all morphological details. This is computationally prohibitive with current day computing facilities. Alternatively, the concept of multi-scale modelling offers significant reprieve from intense micromechanical computing through selective micro-analysis in a very limited region of a macroscopic computational domain. Multi-scale modelling has gained considerable momentum for analysing mechanical response and failure of heterogeneous materials with multiple length scales, e.g. [19–33]. Large domains can be effectively modelled by these methods through information transfer between various scales. Concurrent multi-scale methods implement substructuring and concurrently solve different models at complementary regions of the computational domain corresponding to different resolutions or scales. The two-way coupling of scales by homogenization/localization makes this method suitable for problems involving localization, damage and failure [34]. Macroscopic analysis, using bottom-up homogenization in regions of homogeneous deformation, enhances the efficiency of the computational analysis. On the other hand, top-down coupling with pure microscopic analysis is facilitated by cascading down to the microstructural level at critical regions of localized damage, fracture or instability.

A schematic of the concurrent multi-level computational framework developed in [20–22] for multi-scale modelling of heterogeneous materials is shown in figure 1. The models undergo domain partitioning based on the evolution of stresses, strains and/or damage

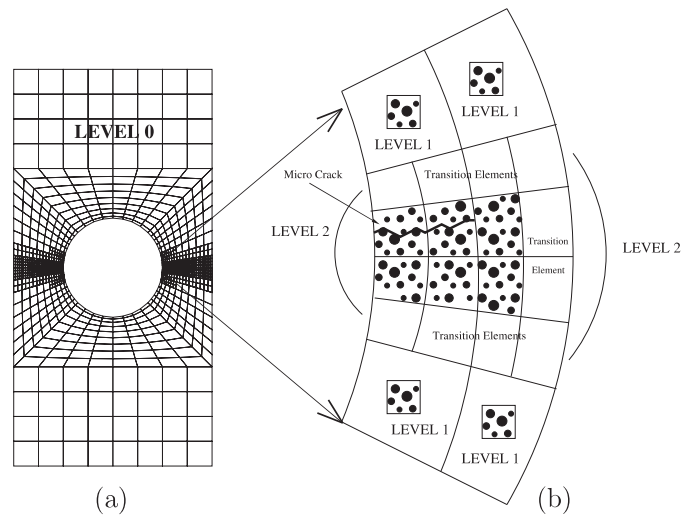


**Figure 1.** Schematic of a coupled concurrent multi-level model showing (a) *level-0* region of macroscopic continuum analysis with adaptive mesh refinement and zoom-in and (b) blow-up of critical region containing *level-1* (swing region with RVE analysis) and *level-2* (region of pure micromechanical analysis).

in the microstructure. An optimal domain partitioning can significantly enhance the efficiency of multi-scale computational models by keeping the ‘zoomed-in’ regions of intense micromechanical analysis to a minimum. A challenge in the implementation of the multi-scale modelling method for structures with non-uniform microstructure is the delineation of computational substructures based on morphological information and properties at different scales. Some multi-scale models, e.g. in [20, 22, 32] have assumed periodic repetition of microstructural representative volume elements or RVEs over the entire computational domain. The RVEs themselves can contain a reasonably large number of heterogeneities ( $\sim 100$ ). An underlying assumption in these models is that the microstructural morphologies do not exhibit strong irregularities to prevent homogenized representation of the computational domain. Subsequently, micro-domains emerge as a consequence of evolution of local response variables such as stresses and strains. However, the local morphology in many non-uniform heterogeneous materials may warrant embedding pockets of microstructural regions in an otherwise homogenized domain, even prior to starting the analysis. In a concurrent multi-scale model, it is therefore prudent to partition the initial computational domain based on information of the underlying microstructure, prior to mechanical analysis. The morphology based domain partitioning (MDP) is intended for two reasons: (1) to determine microstructural RVEs that can be used in the ‘bottom-up’ homogenization for different regions in the computational domain and (2) to identify those regions where the morphology alone (e.g. regions of dense clustering) can cause a breakdown in the homogenization assumption. Embedded regions requiring microstructural analysis should then be coupled with complementary regions of homogenized macroscopic analysis.

A necessary requirement of the MDP process is that accurate information of the microstructural morphology, at least with respect to certain characterization functions, be available at all points of the computational domain. This can be a very challenging and time-consuming task, if the entire image has to be acquired by optical or scanning electron microscopy. A few methods have been suggested in the literature for dealing with this problem.

A method of preparing a montage of a large number of high magnification microstructural images (nearly 400–500) followed by image compression has been proposed by Gokhale *et al* [12, 35]. Their M-SLIP method is effective for small domains where few images are necessary and the microstructural information obtained has been shown to be sufficient for evaluating point statistics in [36]. However, this process of extracting microstructural images at each individual point may be prohibitively exhaustive for large domains. The  $n$ -point statistics based stochastic image reconstruction techniques have also been used in practice. These involve generating characteristic functions of the morphology, e.g. the lineal path function and using these functions to regenerate the microstructure through a process called simulated annealing (SA) [37–39] by fixing the area fraction and  $n$ -point statistics. Though this method has an advantage of using as many correlation functions as desired, it needs many iterations to evolve towards the expected microstructure and monotonic convergence may not be achieved if the parameters of simulated annealing are not appropriately designed. This may limit its application in reconstructing large microstructural domains. Kumar *et al* [40] have proposed a variant to SA-based statistically equivalent microstructure reconstruction containing potential ‘hot spots’ of high stress or strain localization. Other statistical methods of microstructure reconstruction include random generation of points in a large domain by representing the centroids of second-phase particles followed by replacing each of these points with a particle of a definite shape [41]. A low probability exists that the simulated microstructure will accurately represent features of the actual microstructure, due to the random generation process. Similar methods include the random sequential packing algorithm (RSA) introduced in [42] for simulating dispersions of regular shape particles and the Monte-Carlo technique in [43]. All these methods have shortcomings with respect to convergence to the actual image. There are also few training based techniques such as example based super-resolution in [44], where high frequency bands of sample images at high resolution are used as training sets to enhance the regular interpolated image. However, the method enhances the surface texture rather than the particle features.

The MDP process for multi-phase materials is developed in the present study to create a MDP partitioning as a pre-processor to multi-scale analysis of cast aluminium alloys used in the automotive industry. The overall MDP process consists of three steps, executed in sequence.

- (a) The first step is to simulate necessary high resolution microstructural information at all points of a computational domain from continuous low resolution images of the entire domain and few sample high resolution images. The microstructure image representation and reconstruction method is discussed in section 3.
- (b) The second step, discussed in section 5, uses quantitative characterization of the microstructure using functions of phase distribution, to create effective metrics that can relate microstructural features to critical material behaviour of the aluminium alloys for different secondary dendrite arm spacings or SDAS. Effective parameters are identified for quantifying morphological characteristics based on micromechanical response analysis of various simulated micrographs.
- (c) The third step invokes domain partitioning based on functions of the identified microstructural descriptors. The MDP process delineates regions corresponding to different length scales.

The efficacy of the MDP process is demonstrated for the aluminium alloy microstructures in section 7.

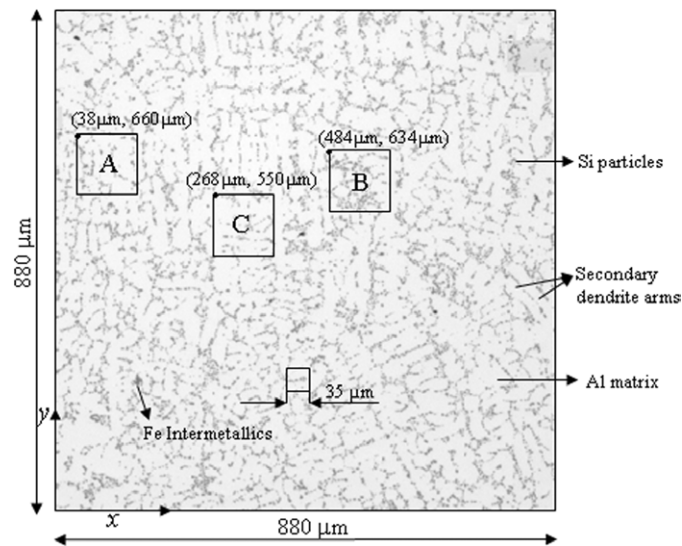


**Figure 2.** Low-magnification, low-resolution digital image of cast aluminium alloy W319, for which high resolution micrograph of a window C is desirable with available high resolution micrographs at other locations A and B.

## 2. Materials Analysed

A scanning electron microscopy (SEM) image of the cast aluminium alloy W319 microstructure, considered in this paper, is shown in figure 2. The aluminium alloy W319 is a higher silicon version of the AA319 alloy, having a nominal composition of Al–7%Si–3%Cu–0.4%Fe; it is a typical alloy used for a number of automotive components such as engine blocks. The dark particles in figure 2 are silicon particles while the grey particles represent intermetallics. Two types of intermetallic particles are predominantly found in the W319 aluminium alloy: (i) iron-based intermetallic particles, which are found in the form of acicular platelets, and (ii) copper-based intermetallics that form blocky plates in the inter-dendritic network. The rate of cooling in the casting process has a strong influence on the spatial dispersion of these second-phase particles and intermetallics. The solidification process tends to push the silicon particles into the regions between the secondary aluminium dendrites that are being formed. Once the eutectic temperature is passed, the silicon particles are fixed in location. Hence, the presence of silicon particles indicates the boundaries between two adjacent secondary aluminium dendrite arms. The distance between two arms represents a characteristic feature of the solidification process. This distance is directly related to the cooling rate during solidification and is measured as secondary dendrite arm spacing (or SDAS). In addition to affecting the SDAS, the cooling rate can also significantly affect the size, shape and distribution of the silicon particles, the intermetallic particles and any porosity present. The W319 alloy examined in this paper is intentionally cast to produce microstructures with three different SDAS values  $23 \mu\text{m}$ ,  $70 \mu\text{m}$  and  $100 \mu\text{m}$ , respectively.

## 3. Reconstructing high resolution microstructures from low resolution micrographs

A prerequisite for creating the MDP of the computational domain as a pre-processor for multi-scale modelling is information of high resolution microstructure at all points of the

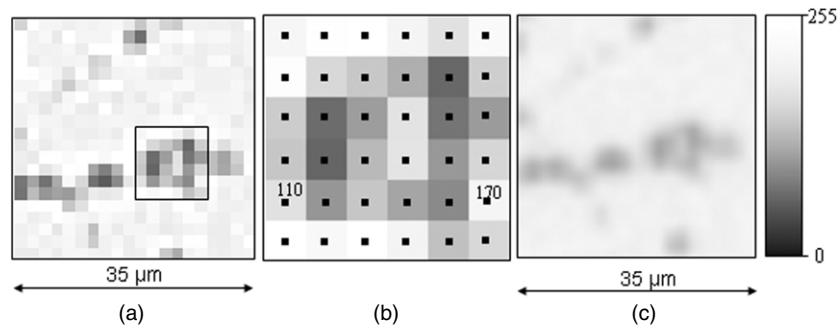


**Figure 3.** High magnification  $35 \mu\text{m} \times 35 \mu\text{m}$  images of a region near C, shown in figure 2: (a) zoomed-in image showing larger pixels but with original resolution; (b) pixel representation of the square region marked in (a); (c) a higher resolution micrograph of (a) obtained by interpolation.

domain. Since it is almost impossible to experimentally obtain contiguous high resolution microscopic images at all points, it is desirable to simulate the local microstructure from micrographs extracted at a few selected locations in the domain. The simulated micrographs should be accurate with respect to important morphological characteristics when compared with the actual micrograph. This section discusses a methodology for simulating such high resolution microstructures at all locations in a low resolution micrograph from detailed high resolution microstructural images at a few sample points. The technique is applicable to optical microscopy or SEM-based micrographs of the alloys. A typical low resolution image of W319 is shown in figure 2. The low resolution micrograph does not provide adequate information required for microstructural characterization and modelling. The microstructure reconstruction process generates corresponding high resolution images with clear delineation of the multi-phase morphology.

The digital micrograph of figure 2 can be resolved into a grid of pixels, with each pixel belonging to a certain level in the greyscale (white–black) hierarchy. For a region  $\Omega_{\text{mic}}$  in the micrograph, the greyscale level of each pixel at  $(x, y)$  is represented by an integer-valued indicator function  $I^g(x, y)$ . For a typical 8-bit monochrome greyscale image, the function is defined as

$$I^g(x, y) = \{p : 0 \leq p \leq 2^8 - 1; \forall (1 \leq x \leq M); (1 \leq y \leq N) \in \Omega_{\text{mic}}\}, \quad (1)$$

i.e.  $I^g(x, y)$  can assume any integer value between 0 and 255 levels at each point of the micrograph. A magnified image of a small region of this micrograph is shown in figure 3(a). In this paper, magnification refers to the pixel size and hence a magnified image will have a larger size of pixels with the same number of greyscale pixels as the original image. Resolution, on the other hand, corresponds to the number of pixels or pixel density in an image. Hence, a higher resolution image will have a higher pixel density with altered greyscale levels. Thus, the number of pixels in the local image of figure 3(a) is the same as that in the original image window of figure 2, with enlarged pixels. Lower pixel densities in the low resolution images result in loss of information on the real image. The microstructure reconstruction method is intended for providing this additional information based on data obtained from a few non-contiguous high resolution images. Various augmentation methods have been proposed in the literature. Polynomial interpolation methods for subpixel values in digital images are developed in [45], but they do not consider simultaneous greyscale variations in two orthogonal directions. Higher order interpolation by the B-spline kernel method [46] provides a more continuous representation of microstructural image, but the interpolated micrographs

are sometimes blurred as shown in figure 3(c). Directional methods [47] interpolate along the edges of discontinuities rather than across them, which reduces the blurring effect. However, the computational efforts incurred in these methods are very high in comparison with the improvement they provide over interpolation methods. Wavelet-based approaches have also been pursued for local interpolation [48]. The high resolution microstructure reconstruction used in this paper incorporates a wavelet-based interpolation of low resolution images that is followed by a gradient-based enhancement method. Numerical experiments conducted show that the *wavelet-based interpolation with gradient-based enhancement or (WIGE) algorithm* enjoys superior convergence characteristics over pure polynomial based interpolation methods.

### 3.1. Wavelet based interpolation in the WIGE algorithm

In the WIGE image reconstruction technique, the integer indicator function  $I^s(x, y)$  in equation (1) is first interpolated in real space using a basis of wavelet functions. Let a window  $\Omega_w^{\text{lrsm}}$  of the low resolution image encompass a  $p \times q$  pixel grid. For a higher resolution image  $\Omega_w^{\text{hrsm}}$ , the same window may contain a  $p' \times q'$  pixel grid, where  $p' > p$  and  $q' > q$ . The greyscale level of each pixel in the  $p \times q$  pixel grid corresponds to the value of the indicator function  $I^s(x, y)$  at its centroid, which is thus represented by known discrete values at a set of equi-spaced points in the low resolution image window. This is shown in figure 3(b). Wavelet-based interpolation is used for estimating the indicator functions ( $I_{\text{wvlt}}^{g'}(x, y) \in R$ ) in the high resolution  $p' \times q'$  pixel grid, where  $R$  is the space of real numbers bounded by 0 and 255. Gaussian functions with continuous derivatives are popular wavelets bases [49, 50] and can effectively represent sharp variations in image features. The Gaussian function is of the form

$$\Phi_{m,n,k,l}(x, y) = e^{-\frac{1}{2}(\frac{x-b_n}{a_m})^2} e^{-\frac{1}{2}(\frac{y-d_l}{c_k})^2} \beta_{m,n,k,l}. \quad (2)$$

Here  $(m, k)$  refer to the wavelet level in a multi-resolution wavelet representation and  $(n, l)$  correspond to the discrete translation of the bases in  $x$  and  $y$  directions, respectively. The parameters  $b_n, d_l$  correspond to translation, while  $a_m, c_k$  are dilation parameters. In encoding a  $p \times q$  pixel subregion of a low resolution image, the indicator function may be expressed in terms of a level  $(m, k)$  Gaussian wavelet function as

$$I_{\text{wvlt}}^{g'}(x, y) = \sum_{1 \leq i \leq p} \sum_{1 \leq j \leq q} \Phi_{m,i,k,j}(x, y). \quad (3)$$

This yields a continuous interpolated image representation in terms of indicator function values of the low resolution image. The bases are constructed by translation from one pixel to the next in the  $p \times q$  pixel subregion and the region is encoded with  $p \times q$  Gaussian functions. The wavelet coefficients  $\beta_{m,n,k,l}$  can be obtained by solving the matrix equation

$$\{I^s\} = [F]\{B\}, \quad (4)$$

where  $\{I^s\}$ ,  $[F]$  and  $\{B\}$  are matrices of order  $pq \times 1$ ,  $pq \times pq$  and  $pq \times 1$ , respectively. The matrix  $\{I^s\}$  contains the values of the indicator functions from the available  $p \times q$  pixel data. The matrix  $[F]$  contains the terms  $e^{-1/2(x_i-b_n/a_m)^2} e^{-1/2(y_j-d_l/c_k)^2}$ ,  $1 \leq i \leq p$  and  $1 \leq j \leq q$  in equation (2), while the matrix  $\{B\}$  contains the unknown wavelet coefficients.

Very large values of  $p$  and  $q$  can lead to numerical instabilities in the solution of coefficients due to nearly linearly dependent columns in  $[F]$ . Numerical studies conducted have indicated that the values for which the system is stable are around  $p = 6, q = 6$ . Consequently the low resolution image is subdivided into basic building blocks that contain a maximum of  $6 \times 6$  pixels. The interpolated indicator function  $I_{\text{wvlt}}^{g'}(x, y)$  for each block of the window, containing a  $p' \times q'$  pixel grid, is constructed as a piecewise continuous wavelet interpolation function of

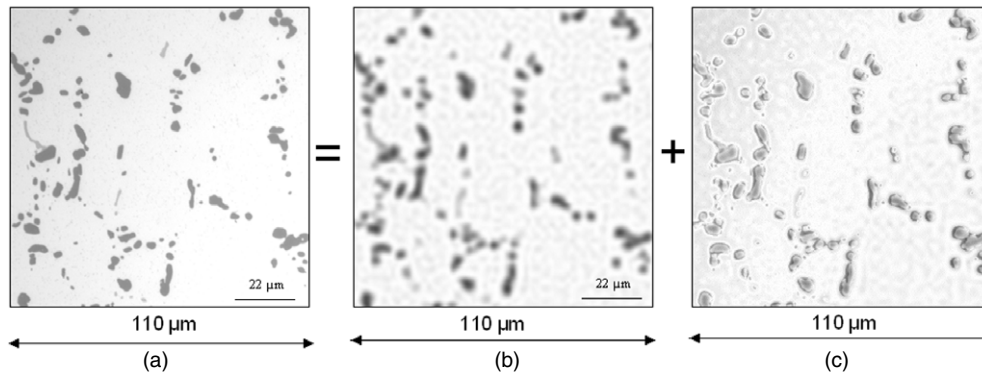


**Figure 4.** High resolution micrographs at location A in figure 2: (a) actual high resolution micrograph; (b) micrograph obtained by wavelet based interpolation in the WIGE algorithm; (c) difference micrograph between (a) and (b).

equation (3). A local coordinate system  $(x, y)$  is set up in each block, with the origin located at its centroid. Consequently, for all blocks of the same  $6 \times 6$  dimension, the matrix  $[F]$  in equation (4) will be identical. Hence, it needs to be computed only once irrespective of the size of the image to be reconstructed.

The interpolation method is tested on the low resolution window marked A in the W319 micrograph of figure 2. The dimensions of the entire micrograph and an image window to be processed are  $880 \mu\text{m} \times 880 \mu\text{m}$  and  $110 \mu\text{m} \times 110 \mu\text{m}$ , respectively. Magnified image of the image window marked A consists of a  $60(=p) \times 60(=q)$  pixel grid. Consequently, there are  $10 \times 10$  blocks containing  $6 \times 6$  pixel grids each in this image window. A high resolution SEM micrograph at the same location is shown in figure 4(a), which has a  $480(=p') \times 480(=q')$  pixel grid, corresponding to a 64-fold increase in the pixel density. The reconstructed image will also have the same pixel density as the high resolution image. The wavelet interpolated image on the  $480 \times 480$  pixel grid is depicted in figure 4(b). A pixel by pixel subtraction of  $I_{\text{wvlt}}^{g'}(x, y)$  for image 4(b) from image 4(a) is depicted in figure 4(c). It is clear that interpolation alone is not sufficient for accurate high resolution microstructure and subsequent image enhancement is essential.

### 3.2. Gradient-based post-interpolation enhancement in the WIGE algorithm

The enhancement method is developed to augment the wavelet interpolated micrographs with the aid of pixel data from high resolution calibrating images at a few different locations in the domain. The method accounts for the proximity of the calibrating micrographs to those being simulated. The first step in this method is a pixel by pixel determination of the difference in the image indicator function values, between the high resolution micrograph  $\Omega_w^{\text{hrsm}}$  and the interpolated image  $\Omega_w^{\text{intm}}$  in the high density pixel grid. The difference indicator function is expressed as

$$I_{\text{diff}}^{g'}(x, y) = I_{\text{hrsm}}^{g'}(x, y) - I_{\text{wvlt}}^{g'}(x, y). \quad (5)$$

The difference micrograph  $\Omega_w^{\text{diff}}$ , corresponding to the images in figures 4(a) and (b), is shown in figure 4(c).

The augmentation methodology requires the creation of a correlation function between  $I_{\text{diff}}^{g'}(x, y)$  and  $I_{\text{wvlt}}^{g'}(x, y)$  that will predict the high resolution image in  $\Omega_w^{\text{hrsm}}$  from the specific

features of the interpolated image in  $\Omega_w^{\text{intm}}$ . For the interpolated image, the pixel-wise grey-scale level or indicator function and its gradients are considered to be characteristic variables that adequately define the local phase distribution. At a point  $(x, y)$  in the pixel space, the value of  $I_{\text{wvlt}}^{g'}(x, y)$  itself is an indicator of a given phase, while the gradients in the four directions  $(x_+, x_-, y_+, y_-)$  are representative of its extent. A discrete correlation function is created between these characteristic variables of the interpolated image  $\Omega_w^{\text{intm}}$  and the indicator function value  $I_{\text{diff}}^{g'}(x, y)$  of the difference image  $\Omega_w^{\text{diff}}$  at locations where high resolution calibrating micrographs are available. This correlation is expressed in a functional form of the indicator function and its gradients as

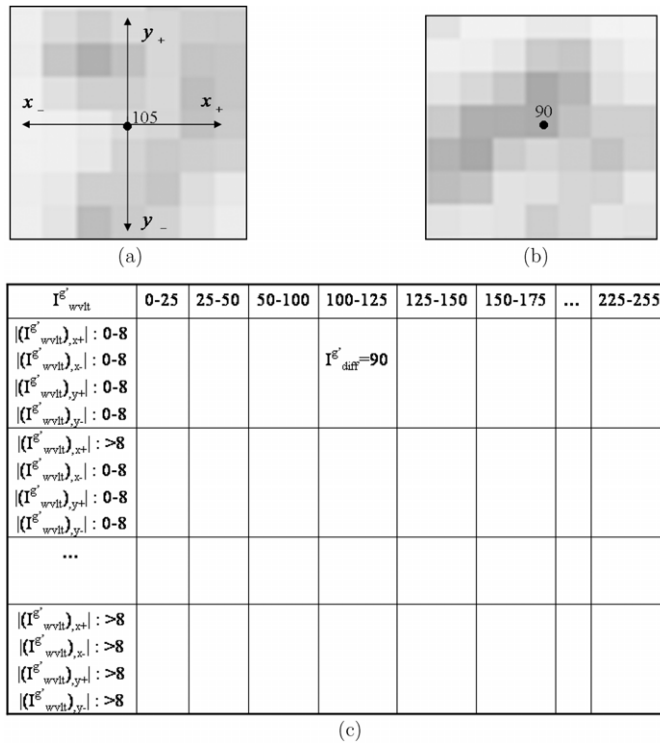
$$I_{\text{diff}}^{g'}(x, y) = P_{\text{diff}} \left( I_{\text{wvlt}}^{g'}(x, y), \frac{\partial I_{\text{wvlt}}^{g'}}{\partial x_+}, \frac{\partial I_{\text{wvlt}}^{g'}}{\partial x_-}, \frac{\partial I_{\text{wvlt}}^{g'}}{\partial y_-}, \frac{\partial I_{\text{wvlt}}^{g'}}{\partial y_+} \right). \quad (6)$$

Here  $P_{\text{diff}}$  corresponds to the most probable or expected value of the difference indicator function and

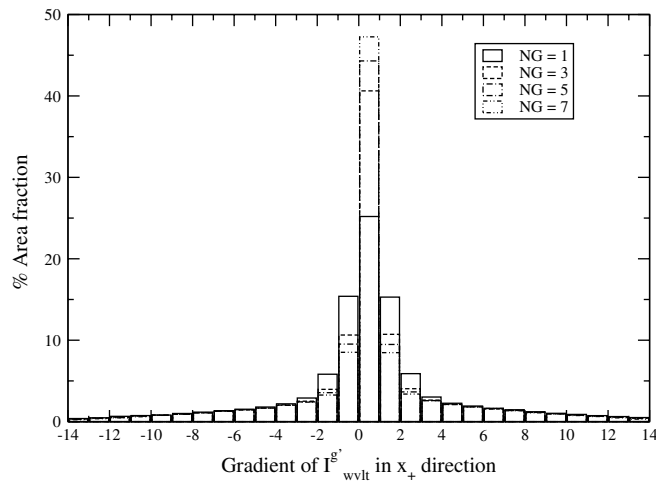
$$\begin{aligned} \frac{\partial I_{\text{wvlt}}^{g'}}{\partial x_{\pm}} &\approx \frac{I_{\text{wvlt}}^{g'}(x \pm \text{NG}, y) - I_{\text{wvlt}}^{g'}(x, y)}{\text{NG}}, \\ \frac{\partial I_{\text{wvlt}}^{g'}}{\partial y_{\pm}} &\approx \frac{I_{\text{wvlt}}^{g'}(x, y \pm \text{NG}) - I_{\text{wvlt}}^{g'}(x, y)}{\text{NG}}, \end{aligned} \quad (7)$$

where NG is the number of pixels over which the gradient may be approximated. The functional form of  $P_{\text{diff}}$  is not known *a priori*. Hence, a discrete probability table is constructed from the calibration micrographs  $\Omega_w^{\text{intm}}$  and  $\Omega_w^{\text{diff}}$  to construct this correlation map. A schematic of the probability table is shown in figure 5. The table is partitioned into discrete boxes or 'bins', based on ranges of  $I_{\text{wvlt}}^{g'}$  and its gradients in four directions, i.e.  $\partial I_{\text{wvlt}}^{g'}/\partial x_+$ ,  $\partial I_{\text{wvlt}}^{g'}/\partial x_-$ ,  $\partial I_{\text{wvlt}}^{g'}/\partial y_-$ ,  $\partial I_{\text{wvlt}}^{g'}/\partial y_+$  in  $\Omega_w^{\text{intm}}$ . These gradients in the bins of the table are expressed with the notation  $\partial I_{\text{wvlt}}^{g'}/\partial x_+ = (I_{\text{wvlt}}^{g'})_{,x+}$ , and so on.

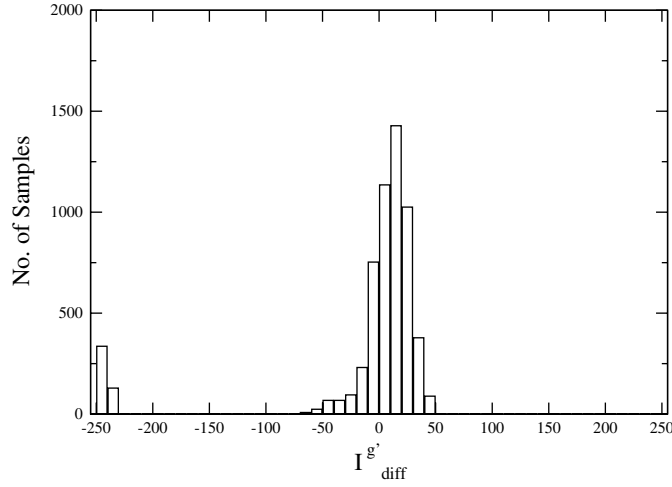
Each bin is represented by a range of values for each of the five variables and contains the values of the difference indicator function  $I_{\text{diff}}^{g'}$  belonging to the difference image  $\Omega_w^{\text{diff}}$ . The range of values to be assigned to each bin depends on the nature of variation of the variables. For example, the range  $0 \leq I_{\text{wvlt}}^{g'} \leq 255$  can be divided into as high as 256 bins or as low as 2 to 3 bins. However, with an increasing number of bins, the number of  $I_{\text{diff}}^{g'}$  entries in each bin will decrease and many of the bins may be empty for the calibration micrographs considered. Sparsity in the correlation bins renders the reliability of this probability table to be low. A moderate number of divisions ( $\sim 10$ – $15$ ) is numerically found to be sufficient, as corroborated by convergence studies discussed later. The range of divisions in the gradients should be such that they are able to distinguish between regions that belong to the interior and exterior of a given phase. A histogram of the distribution in the area fraction of the gradient  $\partial I_{\text{wvlt}}^{g'}/\partial x_+$  for different pixel offset values NG in image 4(b) is plotted in figure 6. Lower values of NG yield a better distribution of the gradients and hence a value of NG = 1 is used in this work. Additionally, the area fractions beyond the bounds  $|\partial I_{\text{wvlt}}^{g'}/\partial x_+| \leq 8$  correspond to the second-phase particles of the microstructure. This conforms to the requirement of delineating regions that belong inside the second-phase particles and, consequently, the range of values for the gradient is separated into two groups: (i)  $|\partial I_{\text{wvlt}}^{g'}/\partial x_+| \leq 8$  and (ii)  $|\partial I_{\text{wvlt}}^{g'}/\partial x_+| > 8$ . The same division is applicable to gradients in other directions too. Figure 5(c) shows the probability table with the discretized ranges of indicator function and its gradients. At a given pixel in  $\Omega_w^{\text{intm}}$  of figure 5(a),  $I_{\text{wvlt}}^{g'} = 105$ ,  $\partial I_{\text{wvlt}}^{g'}/\partial x_+ = 5.0$ ,  $\partial I_{\text{wvlt}}^{g'}/\partial x_- = 4.0$ ,  $\partial I_{\text{wvlt}}^{g'}/\partial y_+ = 3.5$  and  $\partial I_{\text{wvlt}}^{g'}/\partial y_- = 6.5$ . The corresponding  $I_{\text{diff}}^{g'} = 90$  is inserted in the probability



**Figure 5.** Method of correlating interpolated and difference micrographs: (a) an interpolated region, (b) corresponding difference region and (c) table with bins correlating the interpolated micrograph with the difference micrograph.



**Figure 6.** Distribution histogram of the indicator function gradient  $\partial I_{wvlt}^{g'}/\partial x_+$  in the interpolated image of figure 4(b) for various values of NG.



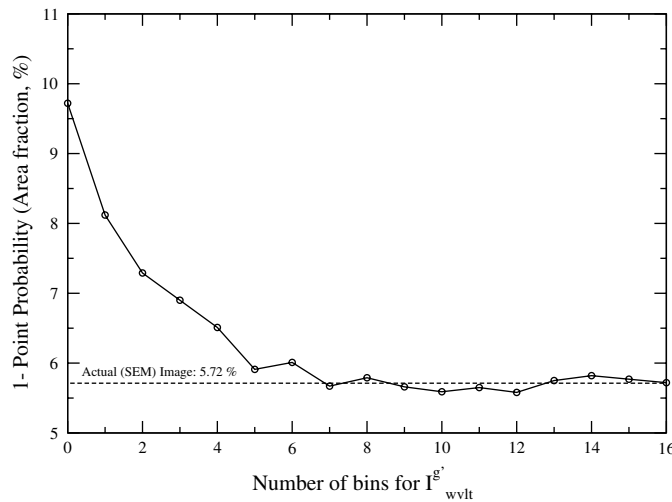
**Figure 7.** A histogram of the distribution of  $I_{\text{diff}}^{g'}$  in the difference image for a given bin corresponding to  $(0 \leq I_{\text{wvlt}}^{g'} < 25, |\partial I_{\text{wvlt}}^{g'}/\partial x_+| \leq 8, |\partial I_{\text{wvlt}}^{g'}/\partial x_-| \leq 8, |\partial I_{\text{wvlt}}^{g'}/\partial y_+| \leq 8, |\partial I_{\text{wvlt}}^{g'}/\partial y_-| \leq 8)$ .

table 5(c). The values of  $I_{\text{diff}}^{g'}$  in the correlation bins vary from location to location for different samples. A histogram of the distribution of  $I_{\text{diff}}^{g'}$  for a given bin corresponding to  $(0 \leq I_{\text{wvlt}}^{g'} < 25, |\partial I_{\text{wvlt}}^{g'}/\partial x_+| \leq 8, |\partial I_{\text{wvlt}}^{g'}/\partial x_-| \leq 8, |\partial I_{\text{wvlt}}^{g'}/\partial y_+| \leq 8, |\partial I_{\text{wvlt}}^{g'}/\partial y_-| \leq 8)$  is shown in figure 7. The peaks in the histogram associate a high probability value of  $I_{\text{diff}}^{g'}$  with that correlation bin. This corresponds to the expected value of  $I_{\text{diff}}^{g'} = P_{\text{diff}}(I_{\text{wvlt}}^{g'}, \frac{\partial I_{\text{wvlt}}^{g'}}{\partial x_+}, \dots)$  that is selected for image enhancement of  $I_{\text{wvlt}}^{g'}$  according to equation (5).

**3.2.1. Accounting for the location of the calibrating micrographs.** For multi-phase microstructures, the location of high resolution calibrating micrographs in relation to the image being simulated is of considerable importance to the image augmentation process. A major assumption made is that if the calibrating micrographs contain the same constituent phases as the ones being simulated and if they are all produced by the same manufacturing process, the probability functions ( $P$ ) of local microstructural distributions will have a continuous variation from one micrograph to the next. These probability-wise similar local distributions are necessary for the calibration process to hold. For sharply contrasting micro-regions, calibrating micrographs should be appropriately chosen from regions that represent the essential features of the one being simulated. The effect of the proximity between calibrating and simulated images can be addressed by assigning distance-based weights to the expected values in the probability table. Micrographs closer to the simulated image will have a stronger influence than those that are farther away. The inverse dependence of a microstructure's correlation map on its spatial distance from each of the calibrating micrographs is represented by a 'shape function' type interpolation relation, commonly used in finite element analysis, i.e.

$$P_{\text{diff}}(x, y) = \sum_{\alpha} N_{\alpha}(x, y) P_{\text{diff}}(x_{\alpha}, y_{\alpha}), \quad (8)$$

where  $\alpha$  is the total number of high resolution calibration micrographs and  $N_{\alpha}$  are the associated shape functions. When only two calibrating micrographs A and B are available as in figure 2,



**Figure 8.** Convergence of 1-point probability function with increasing number of divisions in the range of  $I_{wvlt}^g$  or bins, for the simulated micrograph at region C of figure 2 by the WIGE algorithm.

the most expected value of the enhancement  $I_{diff}^{g'}(x, y)$  at a pixel in the simulated micro-image is obtained as

$$I_{diff}^{g'}(x, y) = P_{diff}(x, y) = \left(\frac{1 - \xi}{2}\right) P_{diff}(x_A, y_A) + \left(\frac{1 + \xi}{2}\right) P_{diff}(x_B, y_B). \quad (9)$$

Here  $\xi = (R_A - R_B)/R_{AB}$  and  $R_A$  and  $R_B$  are the distances of a pixel in the simulated image from the corresponding pixels in calibrating micrographs A and B, respectively, and  $R_{AB}$  is the distance between them. For microstructures containing a single predominant second-phase in the matrix, e.g. Si for cast aluminium alloys, the different locations, e.g. A and B, may have statistically equivalent expected values in the probability table of figure 5(c). In this case, the effect of multiple locations in equation (8) will be minimal.

**3.2.2. A validation test for the WIGE algorithm.** The effectiveness and convergence characteristics of the WIGE algorithm are tested by comparing characteristic metrics of the simulated microstructure with those for a real micrograph at the same location. The  $n$ -point statistics developed in [51] are effective metrics for multi-phase microstructure characterization and are used as validation tools. Specifically, the 1-point, 2-point and 3-point statistics are used for this validation. For the low resolution microstructural region of figure 2, windows at locations A and B are the high resolution calibration micrographs. The WIGE algorithm is used to simulate the image at a window C, for which a high resolution SEM micrograph is available for validation. The 1-point probability function corresponds to the area fraction of the second-phase particles. Its variation is plotted in figure 8 as a function of increasing number of divisions in the range of  $I_{wvlt}^{g'}$  or bins in the probability table. The value at 0 bins corresponds to the micrograph with no enhancement. The simulated area fraction converges to the SEM image area fraction with about 10 discrete divisions or bins. The 2-point probability function is defined as the probability of finding two points at  $r_1(x_1, y_1)$  and  $r_2(x_2, y_2)$  (end-points of a line), separated by a distance  $r = r_1 - r_2$ , in the same phase in the microstructure, i.e.

$$P_{ij}(r) = P\{I^b(x_1, y_1) = 1, I^b(x_2, y_2) = 1\}$$

where  $I^b = 1$  in the given phase and  $I^b = 0$  otherwise. (10)

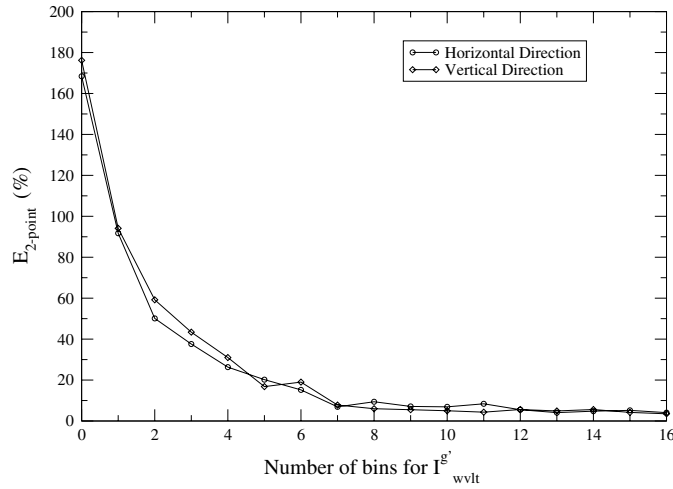


**Figure 9.** Convergence of 2-point probability function with increasing number of divisions in the range of  $I_{wvlt}^{g'}$  or bins, for the simulated micrograph at region C of figure 2 by the WIGE algorithm.

The % error in the 2-point probability function between the actual and simulated images is defined as

$$E_{2\text{-point}} = \frac{\sum_{r=0}^{r=L/2} |P_{ij}^{\text{SEM}} - P_{ij}^{\text{sim}}|}{\sum_{r=0}^{r=L/2} P_{ij}^{\text{SEM}}} \times 100\%. \quad (11)$$

This error is evaluated along two orthogonal directions and plotted in figure 9. Once again, a fast convergence is noted and the error stabilizes to a near zero value for around 10 bins. Finally, the 3-point probability function is defined as the probability of finding three points at  $r_1(x_1, y_1)$ ,  $r_2(x_2, y_2)$  and  $r_3(x_3, y_3)$  (vertices of a triangle) in the same phase, i.e.

$$P_{ijk}(r) = P\{I^b(x_1, y_1) = 1, I^b(x_2, y_2) = 1, I^b(x_3, y_3) = 1\}. \quad (12)$$

$P_{ijk}(r)$  is evaluated for three points at the vertices of an isosceles right triangle with interior angles  $45^\circ$ ,  $45^\circ$ ,  $90^\circ$ . The error in the 3-point probability function is defined in the same way as in equation (11) and is plotted in figure 10. The error in the 3-point probability function also stabilizes to near zero values for  $\sim 10$  bins. The lower order statistics provide information on phase dispersion and are relevant in domain partitioning. Higher order statistics such as the 3-point probability function are important with respect to phase shapes that control the localization and damage behaviour of the material. It may be concluded that the convergence characteristics of the WIGE algorithm are quite satisfactory with respect to 1-point, 2-point and 3-point correlation functions. Excellent agreement can be seen in the WIGE simulated microstructural image and the corresponding actual micrograph shown in figures 11(a) and (b). Thus, this method can be applied sequentially to all windows in the computational domain for obtaining high resolution images.

#### 4. Binary image processing

Prior to characterizing the microstructure of the simulated computational domain, it is necessary to process these images to eliminate noise and clearly delineate dominant phases. Hierarchy in the greyscale levels of digital images may be used for such image processing.

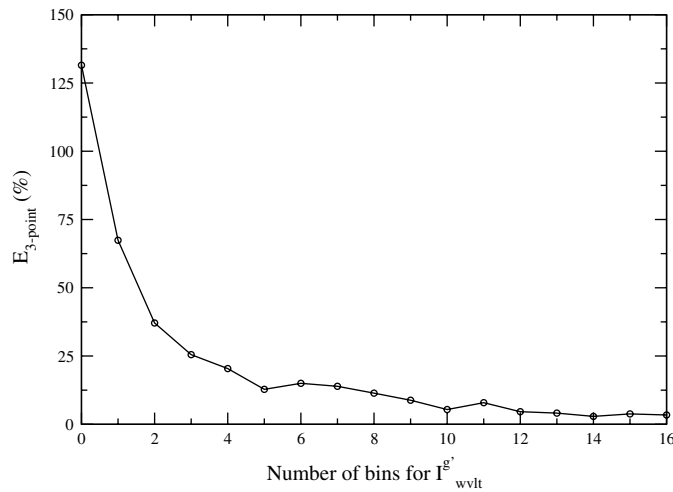


**Figure 10.** Convergence of 3-point probability function with increasing number of divisions in the range of  $I_{wvlt}^g$  or bins, for the simulated micrograph at region C of figure 2 by the WIGE algorithm.

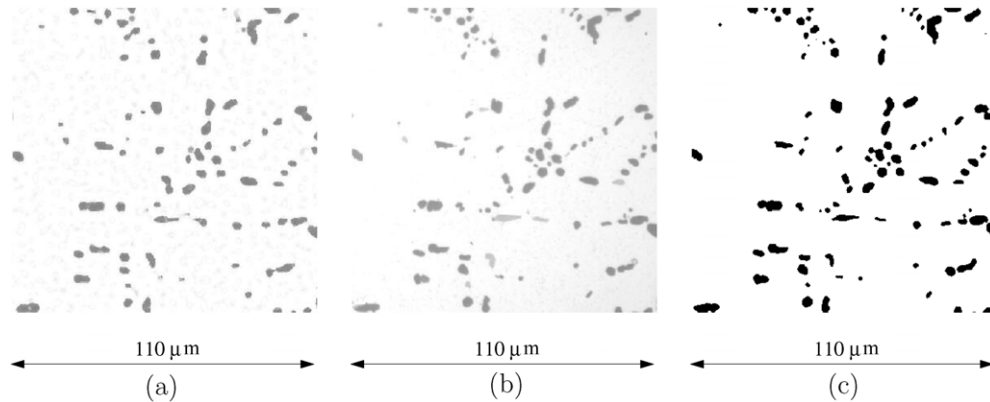


**Figure 11.** High resolution micrograph at location C of figure 2 by the WIGE algorithm: (a) simulated micrograph by using the correlation table, (b) the real high resolution micrograph and (c) binary high resolution micrograph.

During phase delineation, the indicator function values  $I^g(x, y)$  of all pixels belonging to a given phase are assumed to fall within a narrow band of greyscale levels. Global thresholding is first conducted to enable phase delineation or segmentation in the micrographs. In global thresholding,  $I^g(x, y)$  for the entire image is binarized with respect to a single threshold value. On the other hand, different values may be used in local thresholding based on the local variation of  $I^g(x, y)$ . The latter may be necessary for those micrographs where the same phase may have large differences in greyscale level representations at different locations. Global thresholding is deemed sufficient in this work, since the range of greyscale levels of each phase is assumed to have a narrow bandwidth. In a perfect image belonging to two distinct greyscale levels, global thresholding will yield a bimodal histogram of the percentage of pixels as a function of the greyscale levels. Two distinct peaks exist for such a bimodal histogram and the threshold value of  $I^g(x, y)$  corresponds to the valley point between the peaks. However, in real images

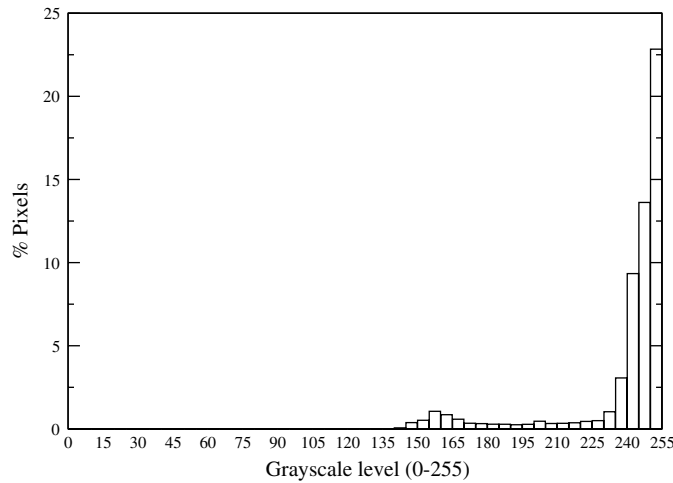


**Figure 12.** Brightness histogram of high resolution micrograph in figure 11(b).

such as in figure 11, histograms are rarely bimodal. Various techniques have been suggested for evaluating the threshold value  $\tau$  for histograms, in which distinct peaks are absent [52,53]. A simple technique is to evaluate  $\tau$  from the shoulder region in the histogram, adjacent to the peak for the matrix phase that has a zero slope. The image can be binarized with respect to the indicator function value as

$$\begin{aligned} I^b(x, y) &= 1 \quad \forall \quad 0 \leq I^g(x, y) \leq \tau \\ &= 0 \quad \forall \quad \tau < I^g(x, y) \leq 2^s - 1. \end{aligned} \quad (13)$$

Heterogeneities (particles or voids) are consequently converted to a black image against a white matrix backdrop. For the W319 micrograph of figure 11(b), a threshold value of  $\tau = 225$  is obtained from the histogram in figure 12. The corresponding binary (black and white) image of the microstructure is shown in figure 11(c). For multi-phase microstructures with more than two phases, more than one threshold is necessary to separate different phases. The distinction between Si particles and intermetallics in cast W319 is not made in the present work, since the focus is on morphology of additional phases for geometry-based image processing.

Frequently, micrographs have significant noise due to tiny erroneous marks. The corresponding indicator functions  $I^g(x, y)$  get transferred to the binary image indicators  $I^b(x, y)$  based on their greyscale value. To prevent this,  $I^g(x, y)$  is convoluted with a mean filter of mask size  $n$  as shown in [54]. The process replaces each pixel at  $(x, y)$  with its respective local average greyscale level. The binary image also often contains tiny speckles due to thresholding. These speckles are unwanted noise and the binary image should be despeckled using a median filter on a kernel of mask size  $m$  pixels. The de-noising kernels help automation of the whole process without any user intervention. The binary domain, derived from this process, represents a high resolution computational domain  $\Omega_{\text{mic}}$  necessary for microstructural characterization and analysis.

## 5. Functions for microstructure characterization

The microstructure simulated in the previous section contains regions belonging to the matrix phase  $\{\Xi_m\}$  and the  $N_c$  heterogeneities, represented as  $\{\Xi_c^i : 1 \leq i \leq N_c\}$ , i.e.

$\Omega_{\text{mic}} = \Xi_{\text{m}} + \sum_{i=1}^{N_c} \Xi_c^i$ . Characterization functions of relevant features and parameters, e.g. those identified in the experimental and numerical studies of [1, 2, 55, 56], are chosen with a focus on material deformation and failure behaviour. For instance, damage in cast W319 occurs by a combination of particle cracking, microcrack formation and growth in the matrix and coalescence of microcracks. Particle cracking depends on size, aspect ratio and the extent of clustering. Bigger particles with high aspect ratio or those within a cluster show a higher propensity towards cracking. Parameter descriptors and characterization functions that are selected to quantify the size or shape of heterogeneities  $\Xi_c^i$  and their spatial distribution in  $\Omega_{\text{mic}}$  are discussed next.

### 5.1. Size descriptors

Descriptors of area, perimeter and longest diameter of the heterogeneities are evaluated from the binary image data  $I^b(x, y)$  in the microstructural image  $\Omega_{\text{mic}}$ , following their definitions.

- (i) *Area* ( $A^i$ ) is measured in terms of the total number of pixels belonging to a heterogeneity  $\Xi_c^i$ :

$$A^i = \int_{\Xi_c^i} I_i^b(x, y) \, dx \, dy. \quad (14)$$

The local area fraction  $A_f^i = A^i / A_{\Omega_{\text{mic}}}$  is a more effective descriptor.

- (ii) *Perimeter* ( $P^i$ ) is measured by the number of pixel-edges in  $\Xi_c^i$  that interface with the matrix  $\Xi_{\text{m}}$  in a digital microstructure.
- (iii) *Longest dimension* ( $d_{\text{max}}^i$ ) is measured as the distance between the two farthest points in  $\Xi_c^i$  and is measured as

$$d_{\text{max}}^i = \text{Max}\{|\bar{r}_{AB}| \quad \forall A(x_a, y_a), B(x_b, y_b) \in \Xi_c^i\}. \quad (15)$$

### 5.2. Shape descriptors

Shape descriptors, such as those prescribed in [54, 57], quantify the shape and surface irregularities of a heterogeneity  $\Xi_c^i$ . The following shape metrics are used for quantifying the cast aluminium alloys.

- (i) *Roundness* ( $\rho^i$ ) indicates how close the shape is to a circle. It is effective for heterogeneities of arbitrary shape for which the aspect ratio is not well defined. For  $\Xi_c^i$ , it is defined as [54]

$$\rho^i = \frac{4A^i}{\pi(d_{\text{max}}^i)^2}. \quad (16)$$

$\rho^i$  varies from 1 for circular shapes to 0 for highly elongated phases.

- (ii) *Edge smoothness* ( $\chi^i$ ) describes surface irregularities, e.g. sharp corners, even if it has an overall high roundness. Form factor is a metric that is defined in [54] to delineate surface irregularities as

$$ff^i = \frac{4\pi A^i}{(P^i)^2}. \quad (17)$$

$ff^i$  is sensitive to surface irregularities and varies from 1 for smooth surfaces to 0 for rough surfaces. It is also affected by the aspect ratio. To understand their effectiveness,  $\rho^i$  and  $ff^i$  of arbitrary shapes created in figure 13 are given in table 1. Though  $ff^i$  for shapes 8 through 11 captures the visible surface irregularities, it is very low for shapes

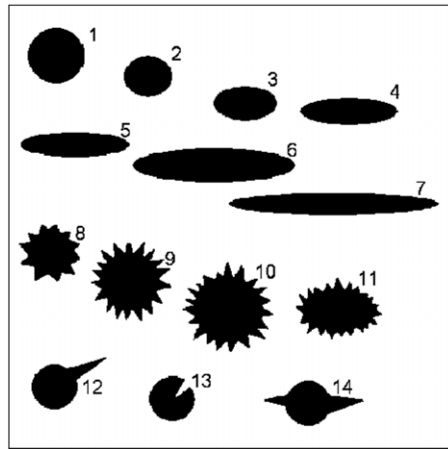


**Figure 13.** Image with simulated heterogeneities for testing the shape description parameters.

**Table 1.** Shape description parameters for image with simulated particles in figure 13.

Particle No.	% Area fraction ( $A_f$ )	Roundness ( $\rho$ )	Form factor(ff)	Edge smoothness ( $\chi$ )
1	1.25	0.9698	0.9909	0.6928
2	0.79	0.8431	0.8631	0.7069
3	0.87	0.5540	0.5559	0.7436
4	1.04	0.2776	0.2776	0.7115
5	1.08	0.2324	0.2325	0.6880
6	2.27	0.2179	0.2179	0.6796
7	1.87	0.1056	0.1073	0.5512
8	1.12	0.6848	0.7317	0.4318
9	1.89	0.6857	0.7193	0.2453
10	2.37	0.6605	0.7094	0.2675
11	1.58	0.5223	0.5495	0.3337
12	0.96	0.3471	0.3655	0.5806
13	0.75	0.9195	0.9274	0.4947
14	1.05	0.2508	0.2694	0.5749

4–7, with smooth surfaces. The edge smoothness  $\chi^i$  is consequently introduced to capture the surface irregularities by de-emphasizing the aspect ratio:

$$\chi^i = \sqrt{ff^i \times \frac{\pi d_{\max}^i}{(P^i)}} = \sqrt{\frac{4\pi^2 A^i d_{\max}^i}{(P^i)^3}}. \quad (18)$$

In  $\chi^i$ , the form factor is amplified by the effect of the largest dimension in the heterogeneity for better representation of surface irregularities. Also, the square root helps in depicting a better separation between different geometries, since the parameter is generally less than 1.  $\chi$  closer to 0 indicates a large number of surface irregularities. However, with the discrete pixel representation of boundaries in a digital image,  $\chi$  can be closer to unity even for a perfect circle.

### 5.3. Spatial distribution descriptors

Spatial distribution, which manifests the relative location of heterogeneities  $\Xi_c^i$  in the matrix  $\Xi_m$ , can be quantified by spatial characterization functions to identify geometric properties such as isotropy, homogeneity and clustering. A wide variety of spatial techniques have been introduced in the literature. These include Voronoi based tessellation techniques in [58–60] for determining probability density functions, pair distribution function distributions for nearest neighbour distances, local area fractions, etc and image-based characterization in [61–63] for evaluating mean free path, nearest neighbour distance and for detecting clusters. The covariance function [64] and other explicit descriptors are incorporated as morphological tools.

**5.3.1. Covariance function.** The covariance function  $K(h)$  is defined in [64] as the Lebesgue measure of a deterministic compact set  $X$  in  $R^n$ , that is eroded by  $B = \{0, h\}$ , which is a set of points at the ends of a vector  $OH$ . For digital images of multi-phase microstructures,  $X$  corresponds to the set of all the points that belong to the heterogeneities and  $B$  is a structural element consisting of two end pixels separated by a distance  $h$  and making an angle ( $\alpha$ ) with the reference axis. For  $\alpha = 0^\circ$  and  $\alpha = 90^\circ$  in the binary digital images, the function can be expressed as

$$\begin{aligned} K(h)_{(\alpha=0^\circ)} &= \text{Mes}(X \ominus B) = \int_{R^n} I^b(x, y) \cdot I^b(x+h, y) \, dx \, dy, \\ K(h)_{(\alpha=90^\circ)} &= \int_{R^n} I^b(x, y) \cdot I^b(x, y+h) \, dx \, dy, \end{aligned} \quad (19)$$

where  $I^b(x, y)$  (see equation (13)) is the binary indicator function of the image associated with the set  $X$  and  $X \ominus B$  indicates the erosion of set  $X$  by the element  $B$ . The set  $X$  in the binary microstructure is defined as  $X = \sum_{i=1}^{N_c} \Xi_c^i = \Omega_{\text{mic}} - \Xi_m$ . The eroded set  $X \ominus B$  may be expressed as  $X \cap X_h$ , where  $X_h$  is a translated set of  $X$ . For any point  $x$ ,

$$x \in (X \ominus B) \quad \text{iff} \quad x, x+h \in X. \quad (20)$$

For  $I^b(x, y) = 1$ ,  $K(h)$  denotes the total number of events for which pixel points  $(x, y)$  and  $(x+h, y)$  both belong to the second-phase particle region. Computationally it is evaluated as the number of particle pixels that overlap when the image is translated by a distance  $h$  at an angle  $\alpha$  to the reference direction and overlaid on itself. The covariance function  $K(h)$ , normalized with the total number of pixels in the micrograph 11(c), is plotted in figure 14 for  $\alpha = 0^\circ$  and  $\alpha = 90^\circ$ . The plots capture the average properties at shorter translations ( $\leq h$ ) as well as the behaviour of the spatial distribution at larger translations. For smaller values of  $h$ ,  $K(h)$  corresponds to the intersection of a particle with its own translated image. Consequently, it decreases rapidly with  $h$  with decreasing self-overlay. The small increase in  $K(h)$  at higher values of  $h$  refers to the intersection with neighbours. Hence, the average nearest neighbour distance  $l_{\text{nd}}$  of a micrograph corresponds to the smallest value of  $h$  at which  $K(h)$  is a local minimum. The first local minima of  $K(h)$  in figure 14 occur at  $9.6 \mu\text{m}$  for  $\alpha = 0^\circ$  and  $8.5 \mu\text{m}$  for  $\alpha = 90^\circ$ . These correspond to the average nearest neighbour distances in the two orthogonal directions.

**5.3.2. Cluster index.** Clustering is manifested by a high local density of heterogeneities in the matrix and often gives rise to local stress concentrations. The W319 micrograph in figure 2 contains large regions of Al matrix surrounded by the silicon particles. This structure is formed by solidification, where the growing aluminium dendrites force the silicon particles

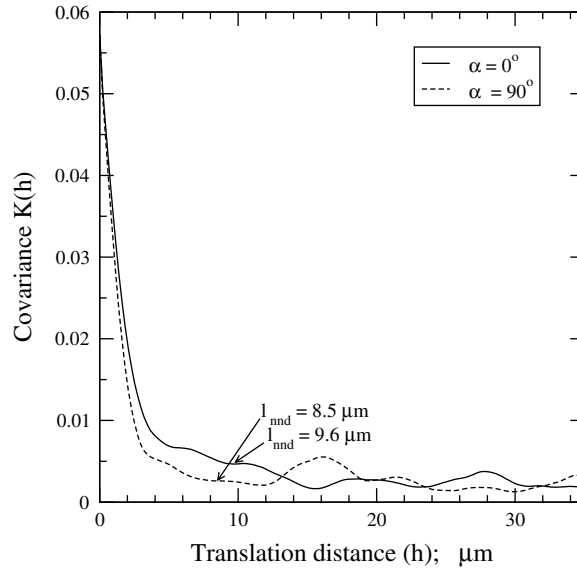


**Figure 14.** Covariance ( $K(h)$ ) plot for micrograph in figure 11(c) along two orthogonal directions.

into the spaces between the dendrite arms. Particulate clustering in solidified aluminium alloy microstructures is thus related to the secondary dendrite arm spacing or SDAS, as well as the number of particles around a particular dendrite arm. The SDAS, measured as the average centre-to-centre distance of the dendrite arms, provides only a general idea about clustering (e.g. regions of higher SDAS have a higher degree of clustering) without any specific local information. For a better quantification of local clustering, two metrics, namely, the *spacing index* (SI) and the *clustering intensity* (CI), are introduced. These metrics quantify the size of the matrix that is free of second-phase particles and the number of particles concentrated in a particular region. These parameters are normalized with respect to a characteristic radius  $R_{ch}$ , defined as

$$R_{ch} = \sqrt{\frac{A_{\text{image}}}{\pi N}}, \quad (21)$$

where  $A_{\text{image}}$  is the image area and  $N$  is the total number of particles.  $R_{ch}$  signifies the inter-particle distance for an ideal distribution of circular particles in the image. SI is a measure of the dendrite arm size, which is estimated as the normalized radius of the biggest circle that can fit into the micrograph without intersecting any particles. However, as shown in figure 15, stray tiny particles in the matrix region can result in lower than reasonable values of the arm size. To prevent this error, the spacing radius is evaluated beyond the first interfering particle to check if the radius increases drastically (at least 25%). In that event, a new radius is used with a compensating multiplication factor for the enclosed particles, i.e.

$$S_{\text{ind}} = \frac{R_{\text{max}}(1 - A_f)}{R_{ch}}, \quad (22)$$

where  $a_f$  is the area fraction of the interfering particle.

CI, on the other hand, quantifies the intensity of packing in a cluster. It is measured as the normalized difference between the maximum and minimum number of particles enclosed

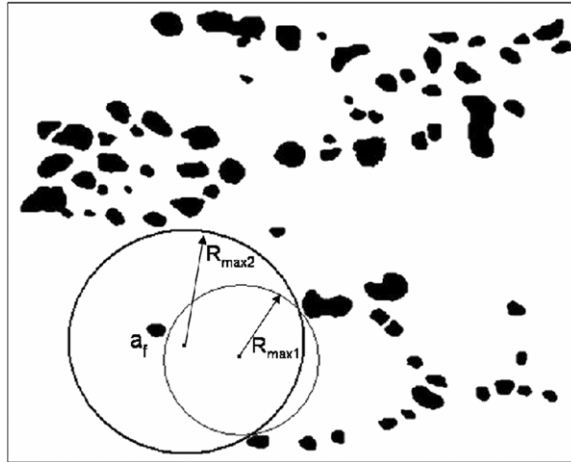


**Figure 15.** Microstructure showing regions that have pockets of few second-phase particles in large matrix regions.

within a characteristic circle with radius  $R_{ch}$ , i.e.

$$CI = \frac{N_{\max}^e(x_{\max}, y_{\max}) - N_{\min}^e(x_{\min}, y_{\min})}{N_{\text{avg}}}, \quad (23)$$

where  $N_{\max}^e$  and  $N_{\min}^e$  are the maximum and minimum number of particles inside the characteristic circle at points  $(x_{\max}, y_{\max})$  and  $(x_{\min}, y_{\min})$ , respectively, and  $N_{\text{avg}}$  is the average number of particles inside the characteristic circle over all points of the micrograph.

Finally, the *cluster index* ( $\kappa$ ), quantifying clustering in a microstructure, is defined as the product of spacing index  $SI$  and the clustering intensity  $CI$ , i.e.  $\kappa = SI \times CI$ . The effectiveness of  $\kappa$  in quantifying spatial distribution is demonstrated later.

**5.3.3. Cluster contour.** Contour plots of parameters that represent local clustering are also helpful in identifying clusters. Such a contour plot can be generated using the characteristic radius  $R_{ch}$  as the field of influence of each heterogeneity. The total area of heterogeneities inside each characteristic circle is measured as contour intensity (COIN) at a point. The cluster contour index  $\iota$  is then defined in terms of the contour intensity as

$$\iota = 1 - \frac{\text{Mean COIN}}{\text{Max COIN}}. \quad (24)$$

The mean and maximum values of COIN are evaluated from all points of the micrograph. A contour index  $\iota = 1.0$  denotes a cluster, while values closer to zero indicate uniform distribution. The contour index accounts for the area fraction of particles within a prescribed region while the cluster index considers the number of particles in this region.

The microstructural descriptors can all be used to quantify the morphology of second-phase particles in a microstructure. In the following subsection their effectiveness in identifying microstructural characteristics of the W319 alloy is discussed.

#### 5.4. Characterization of the W319 microstructure

The materials considered in this paper are the aluminium alloy W319 with different secondary dendrite arm spacing or SDAS that is directly related to the solidification rate. The tensile

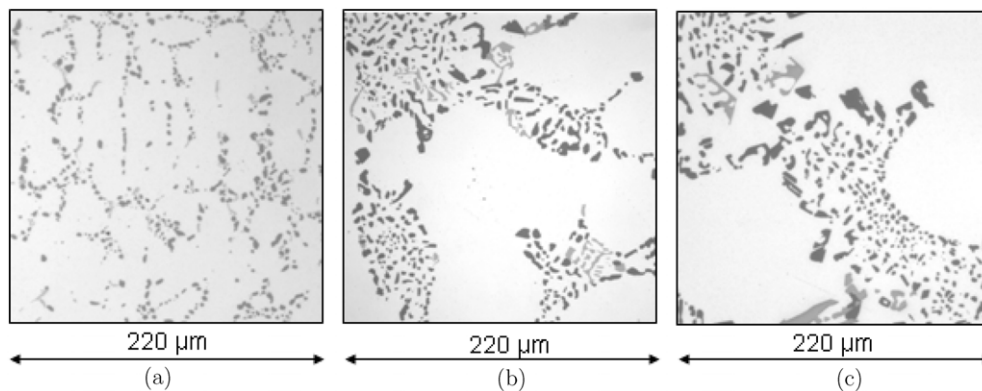


**Figure 16.** W319 micrographs at various SDAS values. (a) SDAS = 23  $\mu\text{m}$ , (b) SDAS = 70  $\mu\text{m}$ , (c) SDAS = 100  $\mu\text{m}$ .

strength and ductility of the material are found to increase with decreasing SDAS [3]. It is important to characterize the microstructure with respect to various size, shape and distribution parameters prior to microstructural modelling to understand their effect on material behaviour and failure response. High resolution W319 micrographs at different SDAS values are characterized in this section to determine the sensitivity of the parameters and functions described in section 5.

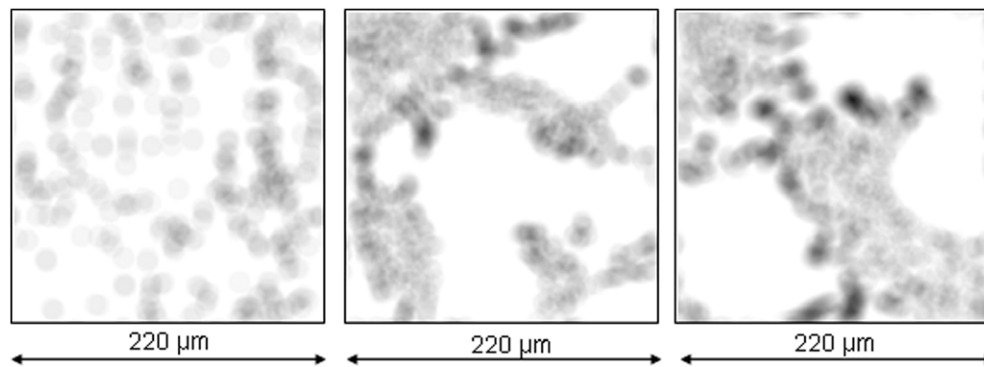
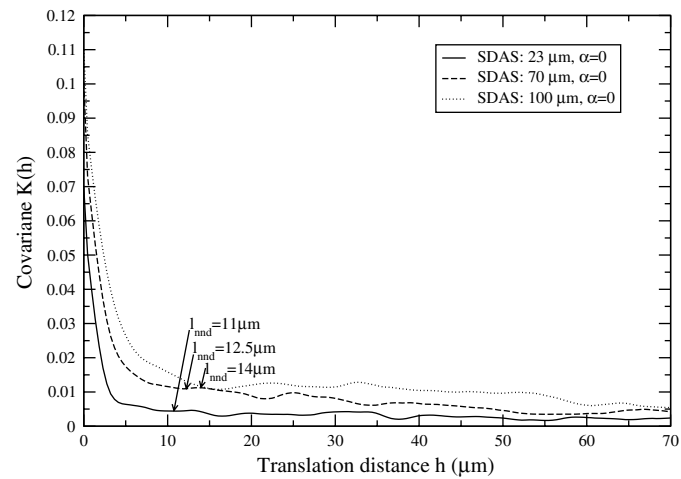
High-resolution, high-magnification micrographs of W319 with average SDAS values 23  $\mu\text{m}$ , 70  $\mu\text{m}$  and 100  $\mu\text{m}$  are shown in figures 16(a), (b) and (c), respectively. The different size, shape and clustering of second-phase particles are evident from these figures. The length scale of the high resolution micrograph is important when comparing the microstructures of different SDAS. At lower length scales, e.g. with a micrograph size of  $\sim 100 \mu\text{m}$ , the 23  $\mu\text{m}$  SDAS microstructure exhibits a clear delineation of particles, while the higher SDAS microstructures may not even contain any particles. At higher length scales of  $\sim 500 \mu\text{m}$ , the resolution diminishes with a loss of feature clarity and hence a micrograph length scale of 220  $\mu\text{m}$  is adopted in this study. Size, shape and clustering parameters for the microstructures in figure 16 are tabulated in table 2. The total area fraction, of silicon particles and intermetallics together, is found to increase with SDAS size. The decreasing roundness and edge smoothness with increasing SDAS, contributed by both silicon particles and intermetallics, capture the acicular shaped particles in higher SDAS material. The cluster index ( $\kappa$ ) and contour index ( $\iota$ ) increase with SDAS, revealing higher particle density at higher SDAS. Cluster contour plots are shown in figure 17, which point to the higher variation of particle distribution with increasing SDAS value. The covariance plot of these micrographs at  $\alpha = 0^\circ$  in figure 18 shows that there is very little difference in the average nearest neighbour distance  $L_{\text{nd}}$ , despite higher levels of clustering at higher SDAS.

### 5.5. Identification of effective spatial distribution descriptors

Multi-scale characterization-based domain partitioning will require effective microstructure descriptors and characterization functions that can establish the relation between morphology and critical material response. Micromechanical damage analyses are conducted in this section for different simulated microstructures and the effectiveness of the spatial distribution functions is studied for their incorporation in domain partitioning criteria discussed in the subsequent sections. Two micro-regions of 10% area fraction and containing 50 identical elliptical particles

**Table 2.** Microstructure characterization parameters for the W319 alloys with different SDAS values, shown in figure 16.

Parameter	23 $\mu\text{m}$ SDAS	70 $\mu\text{m}$ SDAS	100 $\mu\text{m}$ mSDAS
Total $A_f$	6.90%	10.0%	11.0%
Minimum roundness( $\rho$ )	0.285	0.120	0.145
Average roundness( $\rho$ )	0.720	0.476	0.486
Minimum edge smoothness( $\chi$ )	0.369	0.139	0.281
Average edge smoothness( $\chi$ )	0.649	0.597	0.583
Cluster index( $\kappa$ )	14.92	19.12	23.35
Contour index( $\iota$ )	0.81	0.83	0.84

**Figure 17.** Cluster contour plots of W319 micrographs shown in figure 16: (a) SDAS = 23  $\mu\text{m}$ . (b) SDAS = 70  $\mu\text{m}$  and (c) SDAS = 100  $\mu\text{m}$ .**Figure 18.** Covariance function plots for W319 at various SDAS of figure 16.

are simulated, as shown in figures 19(a) (three small clusters) and 19(b) (one large cluster). The micromechanical analysis is performed with the VCFEM [13–16] for elastic–plastic deformation with particle cracking only. The particles are brittle with linear elastic material properties, while the matrix is assumed to be ductile and is modelled by  $J_2$  plasticity theory

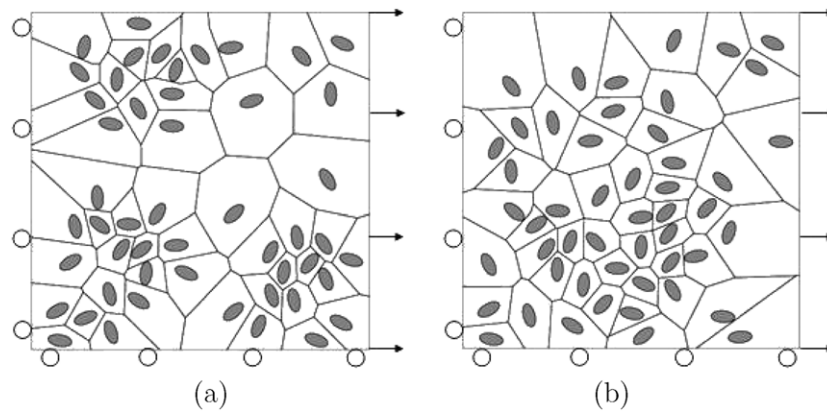


**Figure 19.** VCFEM mesh showing the loading for simulated microstructures for identifying effective spatial distribution parameters: (a) with three small clusters and (b) with one large cluster.

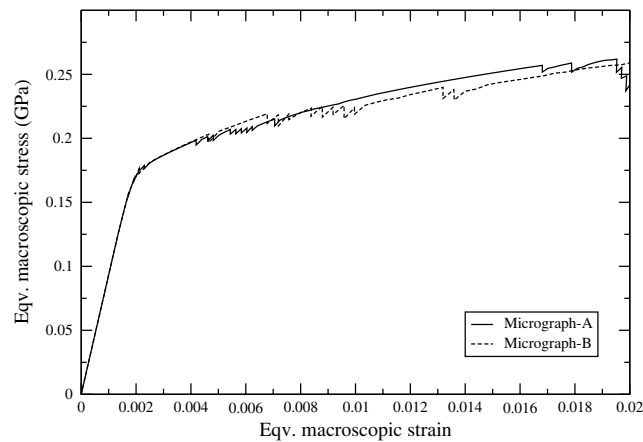


**Figure 20.** Macroscopic stress–strain response for simulated micrographs of figure 19.

with isotropic hardening. For each micrograph, the number of particles that cracked at 2% applied tensile strain is considered as the measure of clustering. The volume-averaged stresses and strains are plotted in figure 20, wherein each drop corresponds to the cracking of one or more particles. The particle cracking initiates earlier at lower values of strain ( $\sim 0.2\%$ ) for micrograph A with three clusters. However, a higher number of cracked particles leading to a higher drop in the stress values is seen for micrograph B with a larger single cluster. The observations are further corroborated in the equivalent plastic strain contour plots of figure 21. In micrograph A, the cracking is predominantly contained within the cluster and does not percolate across the micrograph. However, a dominant path with a higher extent of particle cracking is observed in micrograph B, which causes the increased drop in the stress-carrying capacity. Table 3 shows a comparison of the cluster index ( $\kappa$ ), contour index ( $l$ ) and an inverse nearest neighbour distance ( $1/\hat{L}_{\text{nnnd}}$ ) with the number of cracked particles. The contour index is found to be the best indicator of the trend in the number of particles cracked, for many micro-regions simulated. Hence, the contour index ( $l$ ) is chosen as the spatial distribution descriptor in the MDP process to follow.

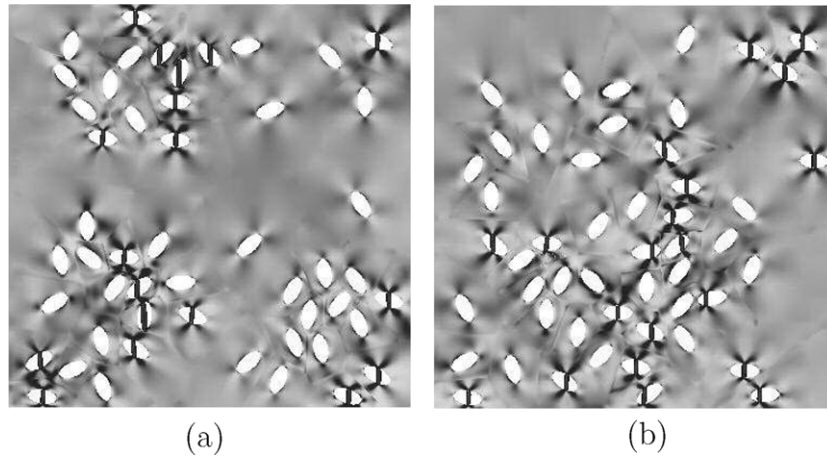


**Figure 21.** Equivalent plastic strain and particle cracking for simulated microstructures of figure 19: (a) with three small clusters and (b) with one large cluster.

**Table 3.** Spatial distribution parameters of two simulated micrographs in figure 19 and the number of simulation based cracked particles at 2% applied strain.

Micrograph	Cluster index( $\kappa$ )	Contour index( $l$ )	$1/\hat{L}_{\text{nd}}$	No. of cracked particles
A	6.68	0.73	20.87	18
B	4.80	0.74	15.82	20

## 6. Domain partitioning as a preprocessor for multi-scale modelling

An assumption made in the concurrent multi-level models of [20–22,34] is that the entire computational domain is initially homogenizable for purely macroscopic computations. However, many heterogeneous materials such as the W319 aluminium alloy have multiple length scales from morphological considerations also (figure 22). Local geometric features render some regions statistically inhomogenizable, i.e. statistical representative volume elements cannot be identified for these regions. Hence, in a true concurrent multi-scale computational model, these regions of geometric non-homogeneity should be identified prior to analysis and concurrently modelled at the microstructural length scales. Once the high resolution microstructural features have been generated for all locations in the computational domain by the WIGE algorithm, the microstructural characterization functions and tools described in section 5 can be used for delineating regions with different scales. The resulting computational domain is expressed as  $\Omega_{\text{comp}} = (\cup_{i=1}^{N_{\text{mac}}} \Omega_{\text{mac}}^i) \cup (\cup_{i=1}^{N_{\text{mic}}} \Omega_{\text{mic}}^i)$ , where the subscripts mac and mic correspond to regions that can and cannot be homogenized, respectively.

The objective of this section is to develop criteria that can enable the pre-analysis partitioning of the computational domain into regions of homogeneity and inhomogeneity. Functions of the microstructure descriptors are developed to establish criteria for successive domain partitioning and refinement.

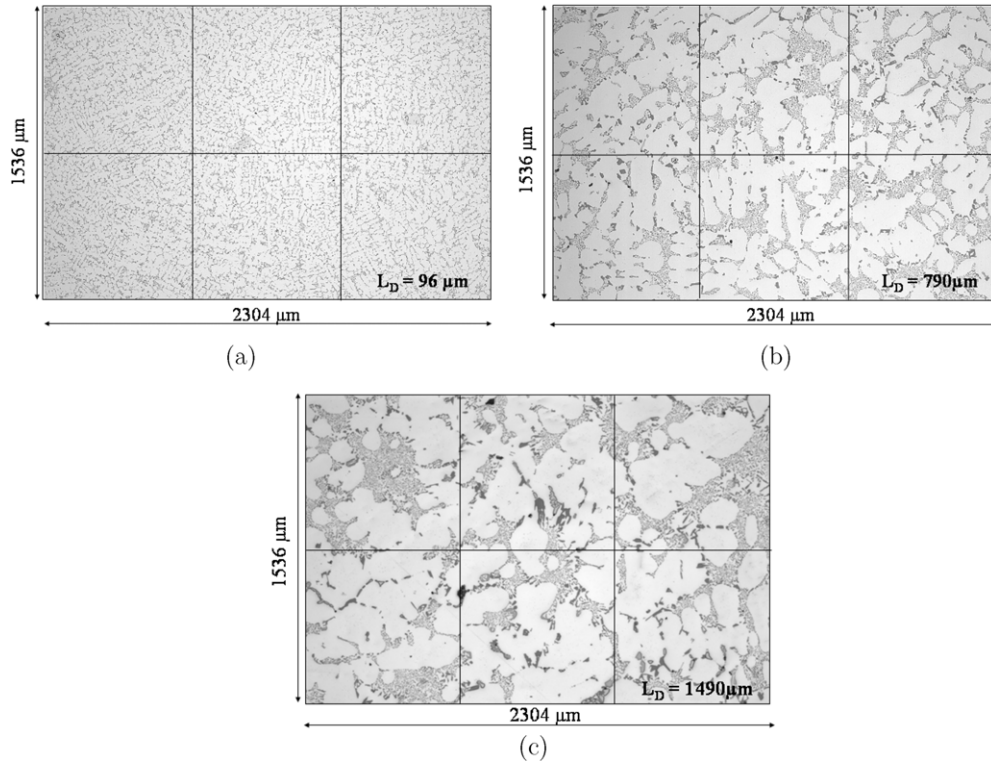


**Figure 22.** Microstructural images of cast aluminium alloy W319 to be partitioned, (a) SDAS = 23  $\mu\text{m}$ , (b) SDAS = 70  $\mu\text{m}$  and (c) SDAS = 100  $\mu\text{m}$ .

### 6.1. Statistical homogeneity and homogeneous length scale ( $L_H$ )

The  $n$ -point probability function  $S_n$  has been introduced in [37], which for a statistically homogeneous media satisfies the condition

$$S_n(x_1, x_2, \dots, x_n) = S_n(x_1 + \bar{x}, x_2 + \bar{x}, \dots, x_n + \bar{x}) = S_n(x_{12}, \dots, x_{1n}) \quad \forall n \geq 1, \quad (25)$$

where  $x_1, x_2, \dots, x_n$  are position vectors of  $n$  points in the medium,  $\bar{x}$  corresponds to a fixed translation and  $x_{ij} = x_j - x_i$ . This implies that for a statistically homogeneous medium,  $S_n$  depends on the relative positions. The 1-point probability function  $S_1$  (the volume or area fraction) is a constant everywhere, i.e. homogeneity can be assumed at regions where  $S_1$  does not vary significantly. A homogeneous length scale  $L_H$  in the material microstructure is established in [65] from this consideration.  $L_H$  is the length scale above which the local variability in area fraction is smaller than a specified tolerance. It is evaluated in the following steps.

- (i) A large high resolution microstructural domain of characteristic dimension  $L$  is divided into finite squares, each of size  $D$ .
- (ii) The area fraction  $A_f$  of the heterogeneities in each square is evaluated. The ratio of standard deviation ( $\sigma_{A_f}$ ) to the mean area fraction ( $\mu_{A_f}$ ) is defined as the coefficient of variation or COV. This corresponds to the variation of  $A_f$  between the squares.
- (iii) The steps 2 and 3 are repeated for different sizes  $D$ .

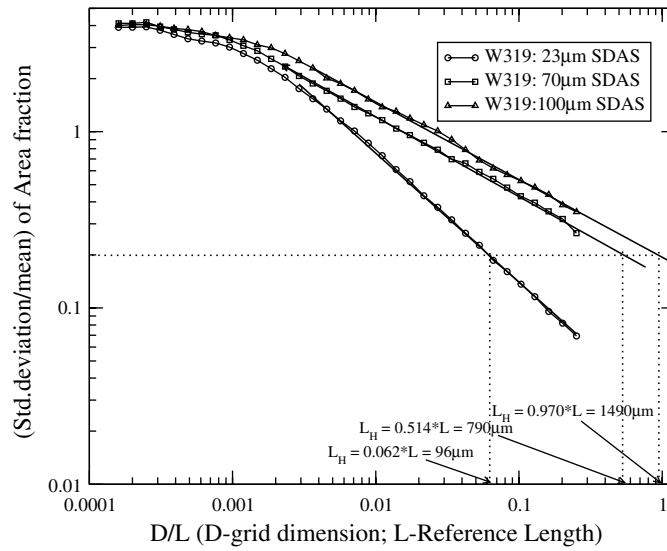


**Figure 23.** Determination of the homogeneous length scale  $L_H$  for W319 with different SDAS values. The figure shows a linear fit in the log scale.

- (iv) For a Poisson distribution, the relation between the COV and the normalized square size  $D/L$  is derived in [65] as

$$\text{COV}(A_f) = \frac{\sigma_{A_f}}{\mu_{A_f}} = \left( \frac{\pi}{4A_f} \right)^{0.5} \left( \frac{D}{L} \right)^{-1}. \quad (26)$$

The corresponding COV varies linearly with the normalized square size  $D/L$  in a logarithmic scale. Hence, the COV for the microstructural image is plotted as a function of  $D/L$  on a logarithmic scale as shown in figure 23.

- (v) The intercept of the plot with the  $D/L$  axis with a preset tolerance is evaluated. The corresponding size  $D$  is identified as the homogeneous length scale  $L_H$ . Below this threshold  $L_H$ , it is necessary to change from a homogeneous to a heterogeneous domain representation with explicit delineation of heterogeneities.

## 6.2. Multi-scale domain partitioning criteria

The **MDP** operation requires the following three ingredients:

- a high resolution microstructure representation for the entire computational domain  $\Omega_{\text{comp}}$ , at least with respect to key characteristic features,
- the homogeneous length scale  $L_H$  and
- representative partitioning criteria in terms of key microstructural descriptors.

Since the extreme values of the microstructural morphology play important roles in the localization and failure behaviour, descriptors that reflect these characteristics are considered important.

The method begins with a coarse discretization of  $\Omega_{\text{comp}}$  into  $N_p^0$  subdomains or partitions, as shown in figure 24(a). A microstructural unit is defined as a high resolution subhomogenization length scale microstructural region  $\Omega_{\text{mic}}$  of dimension  $\xi * L_H$  where  $\xi < 1$ . The factor is chosen as  $\xi = 0.5$  in this work. Any given subdomain  $i$  is assumed to be made

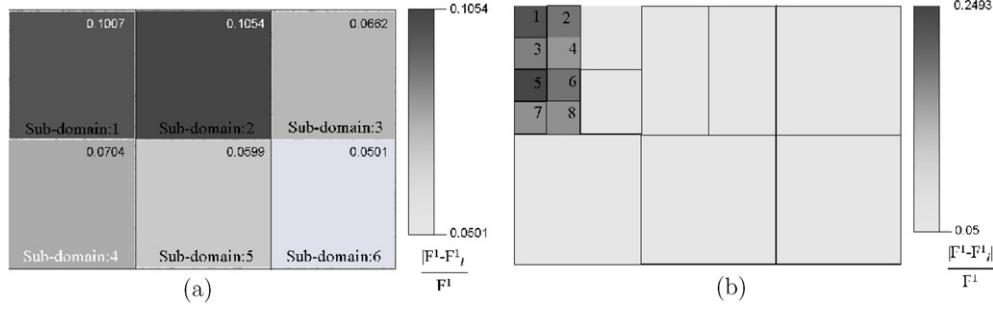


**Figure 24.** Distribution of the partitioning function  $|F^1 - F_{(l)}^1|/F^1$  in the MDP process for W319 SDAS = 23  $\mu\text{m}$ : (a) before first cycle and (b) after the second cycle.

up of  $M^i$  underlying microstructural units. Statistical functions representing the variation of a descriptor in the  $M^i$  microstructural units are evaluated for successive partitioning of a subdomain  $i$ . From the discussions in section 5, the area fraction  $A_f$ , roundness  $\rho$ , edge smoothness  $\chi$  and contour index  $\iota$  are microstructure descriptors that are used construct the refinement criteria functions. Two specific functions are introduced in this work as described below:

- (a)  $F_i^1$ : this function couples the size and distribution descriptors  $A_f$  and  $\iota$ . It is constructed in terms of the mean parameters  $\mu(A_f)$  and  $\mu(\iota)$  for the  $M^i$  microstructural units within each subdomain  $i$  and is expressed as

$$F_i^1 = \mu(A_f)\mu(\iota). \quad (27)$$

- (b)  $F_i^2$ : a function that accounts for both shape and size parameters is defined as

$$S_e = 1 + \sum_{k=1}^{N_c} \left[ \frac{A_f^k}{A_f} (w_\rho(1 - \rho_k) + w_\chi(1 - \chi_k)) \right], \quad (28)$$

where  $A_f^k$ ,  $\rho_k$  and  $\chi_k$  are the local area fraction, roundness and edge smoothness of the  $k$ -th heterogeneity, respectively, and  $A_f$  is the overall area fraction in  $\Omega_{\text{mic}}$ .  $N_c$  is the number of heterogeneities in  $\Omega_{\text{mic}}$  and  $w_\rho$ ,  $w_\chi$  are assigned weights taken as  $w_\rho = 0.5$ ,  $w_\chi = 0.5$ . It should be noted that for microstructures where the aspect ratio or roughness is not pronounced, the value of  $S_e$  tends to 1.0. The contour index ( $\iota$ ) and the overall area fraction  $A_f$  are multiplied with  $S_e$  in the refinement function to capture spatial density of heterogeneities. The resulting function is written as

$$F_i^2 = \mu(S_e \cdot A_f \cdot \iota). \quad (29)$$

The refinement functions  $F_i^k$ ;  $k = 1, 2$  are evaluated in each subdomain, together with those in each of its four divisions  $F_i^k(l)$ ,  $l = 1, \dots, 4$ . A subdomain ( $i$ ) is partitioned only if the following criterion is attained for any of the four subregions:

$$\frac{|F_i^k - F_i^k(l)|}{F_i^k} > C_{f1}, \quad \text{for any } l = 1, \dots, 4. \quad (30)$$

The prescribed tolerance is  $C_{f1} = 0.10$  corresponding to 10% variation.

The successive partitioning process reduces the subdomain size locally and may ultimately reach the homogeneous scale limit  $L_H$ . Once  $L_H$  is reached, only one additional step of further partitioning is possible. The level below  $L_H$  is not homogenizable and hence cannot be refined

any further. A special criterion is required for this partitioning. Each of the subsequent partitions contains only one microstructural unit ( $M^{\text{loc}}$ ) of dimension  $0.5 \times L_H$ . It is not possible to evaluate the statistical functions  $F^k$ ,  $k = 1, 2$  for a single ( $M^{\text{loc}}$ ). The criterion is constructed in terms of the variation of average local area fraction  $A_f$ , an important descriptor that is present in both the functions  $F^k$ ,  $k = 1, 2$ . Partitioning below  $L_H$  is governed by the condition

$$\frac{|(A_f)_i - (A_f)_i(l)|}{(A_f)_i} > C_{f2}, \quad \text{for } l = 1, \dots, 4. \quad (31)$$

Any subdomain below the  $L_H$  threshold is characterized by significant variation in microstructure descriptor functions, e.g. the local area fraction. Consequently, those partitions for which the variation is really large are classified as nonhomogeneous and opened up for explicit microstructural representation in the multi-level model. The factor  $C_{f2}$  is taken as 0.75, corresponding to a 75% difference in the critical regions of the microstructure. The combined microstructure *simulation–characterization–partitioning* method delineates the hierarchy of scales in the computational model as demonstrated in the next simulations.

## 7. Numerical example with the MDP method applied to W319 alloy

The **MDP** methodology is applied to the microstructures of cast aluminium W319 alloy with respective SDAS values of 23, 70 and 100  $\mu\text{m}$ . The low resolution computational micrographs  $\Omega_{\text{comp}}$  of dimensions 2304  $\mu\text{m} \times 1536 \mu\text{m}$  for the alloys are shown in figures 22(a), (b) and (c). The WIGE algorithm generates high resolution images of all points in  $\Omega_{\text{comp}}$  by constructing the correlation table such as that in figure 5, from two 110  $\mu\text{m} \times 110 \mu\text{m}$  high resolution SEM image windows. For the SDAS = 23  $\mu\text{m}$  microstructure, the location of these two windows are shown as **A** and **B** in figure 2. Similar high resolution windows are also considered for 70 and 100  $\mu\text{m}$  SDAS material. The logarithmic scale plot of COV versus  $D/L$  identifying  $L_H$  for the three SDAS is shown in figure 23. The reference dimension is taken as  $L = 1536 \mu\text{m}$  for these plots. The homogenization length scale  $L_H$  is calculated from an intercept tolerance value COV = 0.2 in the log–log plot of figure 23 for the three cases.  $L_H$  increases with the SDAS and consequently larger regions need to be considered for accounting for their natural length scales in the multi-scale modelling process.

The **MDP** process begins by dividing the computational domains  $\Omega_{\text{comp}}$  for each of the three SDAS in figure 22 into 6 subdomains. This initial partition for SDAS = 23  $\mu\text{m}$  is shown in figure 22(a). Successive partitioning progresses according to the refinement criteria in section 6, till the subdomain size reaches  $L_H$ . Figures 24(b) and (d) show the partitioning evolution for three cycles of successive refinement W319 (SDAS = 23  $\mu\text{m}$ ) domain, at which point the  $L_H$  is reached. The corresponding characteristic functions  $|F_i^k - F_i^k(l)|/F_i^k$ ,  $k = 1, 2$  in equation (30) for the first stage are reported in table 4. For the microstructure with SDAS = 70  $\mu\text{m}$ ,  $L_H = 790 \mu\text{m}$ , and for SDAS = 100  $\mu\text{m}$ ,  $L_H = 1490 \mu\text{m}$ . Since the subdomain considered in the first stage of their partitioning is smaller than their respective  $L_H$ , these two domains cannot be partitioned any further beyond the initial partitioning in this example.

The distribution of the characteristic functions  $|F_i^1 - F_i^1(l)|/F_i^1$  for the first and second cycle domain partitioning in the microstructure with SDAS = 23  $\mu\text{m}$  is depicted in the contour plots of figure 24(a) and (b), respectively. The corresponding partitions are shown in figures 25(a) and (b). After the first cycle, partitioning by  $F^2$  deviates from that by  $F^1$ , as observed from the values in table 5. The criterion using  $F^1$  results in 8 partitions, whereas that using  $F^2$  yields 12 partitions based on the  $C_{f1} = 0.1$  cutoff value. The subsequent cycle values of

**Table 4.** Highest values of the refinement functions  $|\mathbf{F}_i^k - \mathbf{F}_i^k(l)|/\mathbf{F}_i^k$  for the first cycle of domain partitioning in W319 (SDAS = 23  $\mu\text{m}$ ) for subdomains 1 through 6 shown in figure 24(a).

Subdomain No.(i)	$ \mathbf{F}_i^1 - \mathbf{F}_i^1(l) /\mathbf{F}_i^1$	$ \mathbf{F}_i^2 - \mathbf{F}_i^2(l) /\mathbf{F}_i^2$
1	0.1007	0.1005
2	0.1054	0.1014
3	0.0662	0.0646
4	0.0704	0.0687
5	0.0599	0.0571
6	0.0501	0.0533

**Table 5.** Highest values of the refinement functions  $|\mathbf{F}_i^k - \mathbf{F}_i^k(l)|/\mathbf{F}_i^k$  for the second cycle of domain partitioning in W319 (SDAS = 23  $\mu\text{m}$ ) for subdomains 1 through 8 shown in figure 25(a).

Subdomain No.(i)	$ \mathbf{F}_i^1 - \mathbf{F}_i^1(l) /\mathbf{F}_i^1$	$ \mathbf{F}_i^2 - \mathbf{F}_i^2(l) /\mathbf{F}_i^2$
1	0.1264	0.1257
2	0.0267	0.0295
3	0.1862	0.1876
4	0.0170	0.0132
5	0.0664	0.0724
6	0.0982	0.1007
7	0.0577	0.0614
8	0.0833	0.0746

$|\mathbf{F}_i^k - \mathbf{F}_i^k(l)|/\mathbf{F}_i^k$  are calculated in table 6 for different  $i$ 's by the two criteria. The subdomain numbers  $i$  are labelled in figures 25(a) and (b) for partitioning by the function  $\mathbf{F}^1$ . The partitioning process continues till the size limit of  $L_H = 96 \mu\text{m}$  is reached. The final partitioned computational domain for SDAS = 23  $\mu\text{m}$  with criteria based on functions  $\mathbf{F}^1$  and  $\mathbf{F}^2$  are shown in figures 25(b) and (c), respectively. Partitioning with  $\mathbf{F}^2$  leads to a higher number of subdomains. At this stage, equation (31) is used for delineating statistically homogeneous regions from inhomogeneous regions. Even with the difference in partitioning, the application of equation (31) yields the same inhomogeneous region in both cases as marked by the  $\mathbf{x}$  in figures 25(b) and (c). The size of the inhomogeneous domain is  $\sim 48 \mu\text{m}$ . The microstructure characteristics of a typical inhomogeneous region  $\mathbf{x}$  and a homogeneous region marked by  $\mathbf{y}$  in figure 25(b) are shown in table 7.

The partitioned domains for SDAS = 70  $\mu\text{m}$  and SDAS = 100  $\mu\text{m}$  microstructures, for which the homogenization length scales  $L_H = 790 \mu\text{m}$  and  $L_H = 1490 \mu\text{m}$ , respectively, are shown in 22(b) and (c). The initial partitioning for these microstructures already brings the size of each partition below  $L_H$ , and hence no additional partitioning is conducted. However, the criterion of equation (31) is applied to each of the six subdivisions of the initial partitioning. For SDAS = 70  $\mu\text{m}$  no regions of statistical inhomogeneity are identified by this criterion. However, five regions are identified for SDAS = 100  $\mu\text{m}$ , as shown in figure 25(d). The inhomogeneous regions identified by the MDP algorithm need to be modeled at the micromechanical level in the concurrent multi-scale analyses and simulations.

## 8. Conclusions

A microstructure MDP methodology is developed in this paper for materials with non-uniform heterogeneous microstructure. The comprehensive set of methods is intended to provide a concurrent multi-scale analysis model with the initial computational domain that delineates

**Table 6.** Highest values of the refinement functions  $|F_i^k - F_i^k(l)|/F_i^k$  for the third cycle of domain partitioning in W319 (SDAS = 23  $\mu\text{m}$ ).

Subdomain No.(i)	$ F_i^1 - F_i^1(l) /F_i^1$	$ F_i^2 - F_i^2(l) /F_i^2$
1	0.2273	0.2250
2	0.1683	0.1708
3	0.1504	0.1207
4	0.1140	0.1178
5	0.2493	0.2772
6	0.1717	0.1691
7	0.1227	0.1146
8	0.1223	0.1369
9		0.1143
10		0.1973
11		0.2102
12		0.2799

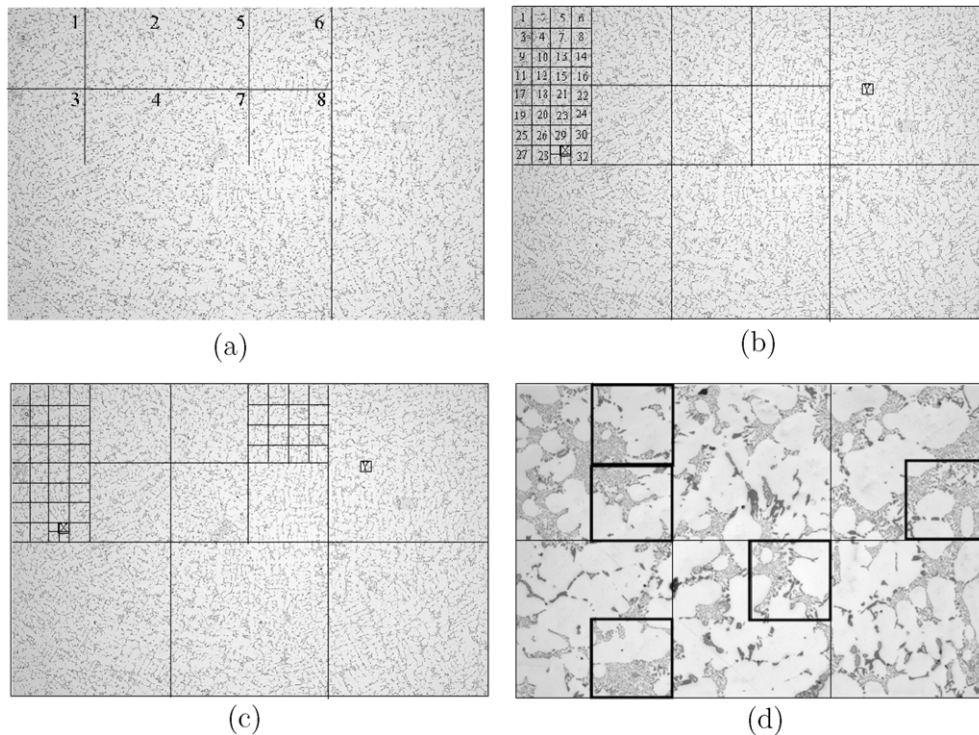


**Figure 25.** Results of the MDP process for the different W319 microstructures: (a) partitioned domain after the first cycle for SDAS = 23  $\mu\text{m}$ , (b) final partitioned domain for SDAS = 23  $\mu\text{m}$  by the  $F^1$ -based criterion, (c) final partitioned domain for SDAS = 23  $\mu\text{m}$  by the  $F^2$ -based criterion, (d) regions of statistical inhomogeneity in the SDAS = 100  $\mu\text{m}$  microstructure.

regions of statistical homogeneity and inhomogeneity. In this sense, the proposed MDP methodology will act as a pre-processor to multi-scale simulation of mechanical behaviour and damage. In this paper, the method is tested on an aluminium alloy W319 with three different secondary dendrite arm spacing or SDAS.

**Table 7.** Comparison of microstructural characteristics of regions marked *X* and *Y* in figure 25(b).

Parameter	Micrograph <i>X</i>	Micrograph <i>Y</i>
No. of particles	26	14
Area fraction $A_f$	11.42%	4.31%
Least roundness $\rho$	0.21	0.41
Least edge smoothness $\chi$	0.37	0.56
Cluster index $\kappa$	7.49	6.40
Contour index $\iota$	0.75	0.72

The **MDP** methodology encompasses a three-step approach to achieve the overall goal. The methods and algorithms are based on geometric features of the morphology without any recourse to mechanical response. In the first step, high resolution microstructural images are simulated from low resolution optical or scanning electron micrographs and a limited set of high resolution micrographs. It incorporates a wavelet interpolation of low resolution images that is augmented by a greyscale gradient-based enhancement algorithm, termed as the WIGE algorithm. The algorithm can overcome the limitations of experimental acquisition of a large set of contiguous micrographs for creating a montage of images in any material domain. In experiments, perfect alignment of the microscope for non-overlapping adjoining domains is a difficult task, aside from the time and expenses incurred in the acquisition process itself. The WIGE algorithm can aid significantly in this acquisition–reconstruction process and is discussed with application for W319 microstructure. Excellent convergence characteristics are observed for the reconstructed W319 micrographs with respect to 1-point, 2-point and 3-point probability functions.

The second step involves the development of microstructure characterization tools that are able to identify morphological features of interest in the multi-scale analysis. The tools incorporate parametric descriptors of size, shape and spatial distributions that directly affect the mechanical and failure behaviour of the material. The descriptors are tested for differentiating the W319 microstructures at three different SDAS, namely,  $SDAS = 23 \mu\text{m}$ ,  $SDAS = 70 \mu\text{m}$  and  $SDAS = 100 \mu\text{m}$ . Micromechanical analyses of particle cracking in simulated microstructures are conducted with the VCFEM. The predictions of the characteristic functions of morphological descriptors are compared with the results of VCFEM simulations. The contour index  $\iota$  is identified to be an effective characteristic function in predicting local damage.

The third and final step is the development of robust multi-scale domain partitioning methods for delineating subdomains corresponding to different scales in concurrent multi-scale analysis. The foremost task is the estimation of a homogeneous length scale or  $L_H$ , below which statistical inhomogeneity is strong to limit the use of homogenization. Following this, two criteria based on different functions of morphological descriptors are developed to govern domain partitioning. Successive domain partitioning continues according to these criteria till the  $L_H$  is reached. Subsequently, a different criterion is invoked to differentiate regions of statistical homogeneity from inhomogeneity. The latter corresponds to regions where explicit representation of the multi-phase microstructure and micromechanical analysis is necessary.

The effectiveness of the **MDP** methodology as a pre-processor for multi-scale analysis of cast aluminium alloy W319 at different SDAS is demonstrated satisfactorily for the numerical examples. The numerical analyses establish distinct requirements on the computational domains for the three SDAS microstructures based on their intrinsic length scales. The computational domains required for successful multi-scale analyses appear to have the same trend as the SDAS. Follow-on work on coupling the multi-scale domain partitioning with

multi-scale analysis is currently underway and will be reported in a future paper. This work is in 2D and will certainly have limitations for those problems that are inherently 3D in nature. However, it presents a framework that can be extended to accommodate three-dimensional problems as long as the necessary 3D tools and accessories are available.

### Acknowledgments

This work has been supported by the National Science Foundation NSF Div Civil and Mechanical Systems Division through the GOALI grant No. CMS-0308666 (Program director: Jorn Larsen-Basse). This sponsorship is gratefully acknowledged. Computer support by the Ohio Supercomputer Center through grant PAS813-2 is also gratefully acknowledged.

### References

- [1] Wang Q G, Caceres C H and Griffiths J R 2003 Damage by eutectic particle cracking in Aluminum casting alloys A356/357 *Metall. Mater. Trans. A* **34** A 2901–12
- [2] Wang Q G 2003 Microstructural effects on the tensile and fracture behaviour of Aluminum casting alloys A356/357 *Metall. Mater. Trans. A* **34** A 2887–99
- [3] James M. Boileau 2000 The effect of solidification time on the mechanical properties of a cast 319 aluminum alloy *PhD dissertation* Wayne State University
- [4] Poole W J and Dowdle E J 1998 Experimental measurements of damage evolution in Al-Si eutectic alloys *Scr. Mater.* **39** 1281–7
- [5] Argon A S, Im J and Sofoglu R 1975 Cavity formation from inclusions in ductile fracture *Metall. Mater. Trans. A* **6** 825–37
- [6] Caceres C H 1999 Particle cracking and the tensile ductility of a model Al-Si-Mg composite system *Aluminum Trans.* **1** 1–13
- [7] Caceres C H and Griffiths J R 1996 Damage by the cracking of silicon particles in an Al-7Si-0.4Mg casting alloy *Acta Mater.* **44** 25–33
- [8] Christman T, Needleman T and Suresh S 1989 An experimental and numerical study of deformation in metal-ceramic composites *Acta Metall. Mater.* **37** 3029–50
- [9] Gonzalez C and Llorca J 1996 Prediction of the tensile stress-strain curve and ductility in Al/SiC composites *Scr. Metall.* **35** 91–7
- [10] Weissenbek E, Boehm H J and Rammerstoffer F G 1994 Micromechanical investigations of fiber arrangement effects in particle reinforced metal matrix composites *Comput. Mater. Sci.* **3** 263–78
- [11] Yang S, Gokhale A M and Shan Z 2000 Utility of microstructure modeling for simulation of micro-mechanical response of composites containing non-uniformly distributed fibers *Acta Mater.* **48** 2307–22
- [12] Shan Z and Gokhale A M 2004 Digital image analysis and microstructure modeling tools for microstructure sensitive design of materials *Int. J. Plast.* **20** 1347–70
- [13] Ghosh S, Ling Y, Majumdar B and Kim R 2000 Interfacial debonding analysis in multiple fiber reinforced composites *Mech. Mater.* **32** 561–91
- [14] Li M, Ghosh S and Richmond O 1999 An experimental-computational approach to the investigation of damage evolution in discontinuously reinforced aluminum matrix composites *Acta Mater.* **47** 3515–52
- [15] Li S and Ghosh S 2006 Extended Voronoi cell finite element model for multiple cohesive crack propagation in brittle materials *Int. J. Numer. Meth. Eng.* **65** 1028–67
- [16] Chao H, Moorthy S and Ghosh S 2004 A Voronoi cell finite element model for ductile damage in MMCs *Materials Processing and Design: Modeling, Simulation and Application: Proc. NUMIFORM (Columbus, Ohio, USA)* ed S Ghosh *et al* (New York: AIP Publishers) pp 1893–99
- [17] Segurado J and Llorca J 2005 A computational micromechanics study of the effects of interface decohesion on the mechanical behaviour of composites *Acta Mater.* **53** 4931–42
- [18] Boehm H J, Han W and Ecksclager A 2004 Multi-inclusion unit cell studies of reinforcement stresses and particle failure in discontinuously reinforced ductile matrix composites *Comput. Modelling Eng. Sci.* **5** 5–20
- [19] Smit R J M, Brekelmans W A M and Meijer H E H 1998 Prediction of the mechanical behaviour of nonlinear heterogeneous systems by multi-level finite element modeling *Comput. Methods Appl. Mech. Eng.* **155** 181–92

- [20] Raghavan P and Ghosh S 2004 Adaptive multi-scale computational modeling of composite materials *Comput. Modelling Eng. Sci.* **5** 151–70
- [21] Ghosh S, Lee K and Raghavan P 2001 A multi-level computational model for multi-scale damage analysis in composite and porous materials *Int. J. Solids Struct.* **38** 2335–85
- [22] Raghavan P and Ghosh S 2004 Concurrent multi-scale analysis of elastic composites by a multi-level computational model *Comput. Methods Appl. Mech. Eng.* **5** 151–70
- [23] Fish J and Shek K 2000 Multiscale analysis of composite materials and structures *Comput. Sci. Technol.* **60** 2547–56
- [24] Fish J, Yu Q and Shek K 1999 Computational damage mechanics for composite materials based on mathematical homogenization *Int. J. Numer. Methods Eng.* **45** 1657–79
- [25] Hao S, Liu W K, Moran B, Vernerey F and Olson G B 2004 Multi-scale constitutive model and computational framework for the design of ultra-high strength, high toughness steels *Comput. Methods Appl. Mech. Eng.* **193** 1865–08
- [26] Hao S, Moran B, Liu W K and Olson G B 2003 A Hierarchical multi-physics model for design of high toughness steels *J. Comput. Aided Mater. Des.* **10** 99–142
- [27] Oden J T and Zohdi T I 1997 Analysis and adaptive modeling of highly heterogeneous elastic structures *Comput. Methods Appl. Mech. Eng.* **148** 367–91
- [28] Vemaganti K and Oden J T 2001 Estimation of local modeling error and goal-oriented adaptive modeling of heterogeneous materials: II. A computational environment for adaptive modeling of heterogeneous elastic solids *Comput. Methods Appl. Mech. Eng.* **190** 6089–24
- [29] Terada K and Kikuchi N 2000 Simulation of the multi-scale convergence in computational homogenization approaches *Int. J. Solids Struct.* **37** 2285–311
- [30] Zohdi T I and Wriggers P 1999 A domain decomposition method for bodies with heterogeneous microstructure based on material regularization *Int. J. Solids Struct.* **36** 2507–25
- [31] Chung P W and Tamma K K 1999 Woven fabric composites: developments in engineering bounds, homogenization and applications *Int. J. Numer. Methods. Eng.* **45** 1757–90
- [32] Xia Z, Curtin W A and Peters P W M 2001 Multiscale modeling of failure in metal matrix composites *Acta Mater.* **49** 273–87
- [33] Xia Z H and Curtin W A 2001 Multiscale modeling of damage and failure in aluminum-matrix composites *Compos. Sci. Technol.* **61** 2247–57
- [34] Raghavan P, Li S and Ghosh S 2004 Two scale response and damage modeling of composite materials *Finite Elem. Anal. Des.* **40** 1619–40
- [35] Gokhale A M and Yang S 1999 Application of image processing for simulation of mechanical response of multi-length scale microstructures of engineering alloys *Metall. Mater. Trans. A* **30** 2369–81
- [36] Tewari A, Gokhale A M, Spowart J E and Miracle D B 2004 Quantitative characterization of spatial clustering in three-dimensional microstructures using two-point correlation functions *Acta Mater.* **52** 307–19
- [37] Yeong C L Y and Torquato S 1998 Reconstructing random media *Phys. Rev. E* **57** 495–505
- [38] Rintoul M D, Torquato S Reconstruction of structure of dispersions *J. Colloid Interface Sci.* **186** 467–76
- [39] Manwart C, Torquato S and Hilfer R 2000 Stochastic reconstruction of sandstones *Phys. Rev. E* **62** 893–99
- [40] Kumar H, Briant C L and Curtin W A 2006 Using microstructure reconstruction to model mechanical behaviour in complex microstructures *Mech. Mater.* **38** 818–32
- [41] Yang N, Boselli J and Sinclair I 2000 Simulation and quantitative assessment of homogeneous and inhomogeneous particle distributions in particulate metal matrix composites *J. Microsc.* **201** 189–200
- [42] Cooper D W 1998 Random sequential packing simulation in three dimensions for spheres *Phys. Rev. A* **38** 522–4
- [43] Everett R K and Chu J H 1992 Modeling of non-uniform composite microstructures *J. Compos. Mater.* **27** 1128–44
- [44] Freeman, Pasztor E C and Carmichael O T 2000 Learning low-level vision *Int. J. Comput. Vision* **40** 24–47
- [45] Robert R K 1981 Cubic convolution interpolation for digital image processing *IEEE Trans. Acoust. Speech Signal Process.* **ASSP-29** 1153–60
- [46] Unser M, Aldroubi A and Eden M 1991 Fast B-spline transforms for continuous image representation and interpolation *IEEE Trans. Pattern Anal. Mach. Intell.* **13** 277–85
- [47] Jensen K and Anastassiou D 1995 Subpixel edge localization and the interpolation of still images *IEEE Trans. Image Process.* **4** 285–95
- [48] Prasad L and Iyengar S S 1997 *Wavelet Analysis with Applications to Image Processing* (Boca Raton, FL: CRC Press)
- [49] Everson R, Sirovich L and Sreenivasan K R 1990 Wavelet analysis of the turbulent jet *Phys. Lett. A* **145** 314–22
- [50] Lewalle J 1994 Wavelet analysis of experimental data: some methods and the underlying physics *AIAA 94-2281, 25th AIM Fluid Dynamics (Colorado Springs)*

- [51] Torquato S 2002 *Random Heterogeneous Materials: Microstructure and Macroscopic Properties* (New York: Springer)
- [52] Sahoo P K, Soltani S and Wong A K C 1988 A Survey of Thresholding Techniques *Comput. Vision Graph. Image Process.* **41** 233–60
- [53] Luthon F, Lievin M and Faux F 2004 On the use of entropy power for threshold selection. *Signal Process.* **84** 1789–804
- [54] Russ J C 1999 *The Image Processing Handbook* 3rd ed (New York: CRC Press and IEEE)
- [55] Caceres C H, Griffiths J R and Reiner P 1996 The influence of microstructure on the bauschinger effect in an Al-Si-Mg casting alloy *Acta Mater.* 1996 **44** 15–23
- [56] Caceres C H, Davidson C J, Griffiths J R and Wang Q G 1999 The effect of Mg on the microstructure and mechanical behaviour of Al-Si-Mg Casting alloys *Metall. Mater. Trans. A* **30** 2611–18
- [57] Michael Seul, Lawrence O’Gorman and Sammon M J 2000 *Practical Algorithms for Image Analysis* (Cambridge: Cambridge University Press)
- [58] Spitzig W A, Kelly J F and Richmond O 1985 Quantitative characterization of second-phase populations *Metallography* **18** 235–61.
- [59] Li M, Ghosh S, Richmond O, Weiland H and Rouns T N 1999 Three dimensional characterization and modeling of particle reinforced metal matrix composites part II: damage characterization *Mater. Sci. Eng. A* **266** 221–40
- [60] Ghosh S, Zdzislaw Nowak and Kyunghoon Lee 1997 Quantitative characterization and modeling of composite microstructures by voronoi cells *Acta Mater.* **45** 2215–34
- [61] Yotte S, Riss J, Breyse D and Ghosh S 2004 PMMC cluster analysis *Comput. Modelling Eng. Sci.* **5** 171–87
- [62] Karnezis P A, Durrant G and Cantor B 1998 Characterization of reinforced distribution in cast Al-Alloy/SiC composites *Mater. Charact.* **40** 97–109
- [63] Anson J P and Gruzleski J E 1999 The quantitative discrimination between shrinkage and gas microporosity in cast aluminum alloys using spatial data analysis *Mater. Charact.* **43** 319–35
- [64] Serra J 1982 *Image Analysis and Mathematical Morphology* (New York: Academic)
- [65] Spowart J E, Mayurama B and Miracle D B 2001 Multiscale characterization of spatially heterogeneous systems: implications for discontinuously reinforced metal-matrix composite microstructures *Mater. Sci. Eng. A* **307** 51–66